Title

Flame Characterization and NOx Emissions Prediction for Reactors Generated by Aeroengine-Derived Lean Direct Injectors, Operated on Hydrogen and Hydrogen/Natural Gas Blends

Permalink

https://escholarship.org/uc/item/5qd992bd

Author

Gomez Escudero, Iker

Publication Date

2023

Peer reviewed|Thesis/dissertation

UNIVERSITY OF CALIFORNIA,
IRVINE

Flame Characterization and NOx Emissions Prediction for Reactions Generated by
Aeroengine-Derived Lean Direct Injectors, Operated on Hydrogen and Hydrogen/Natural Gas Blends

THESIS

submitted in partial satisfaction of the requirements
for the degree of

MASTER OF SCIENCE

in Mechanical and Aerospace Engineering

by

Iker Gomez Escudero

Thesis Committee:
Professor Jack Brouwer, Chair
Professor Vincent McDonell
Professor Bihter Padak

2023

Table of Contents

List of Figures

List of Tables

List of Abbreviations and Symbols

Volumetric flow rate

Uncertainty

Equivalence ratio

Adiabatic flame temperature

Analysis of variance

Background-oriented schlieren

Charge-coupled device

Complementary metal-oxide semiconductor

Center of gravity

Fuel-to-air ratio

Gas turbine

Intensified charge-coupled device

Inner diameter

Knife edge

Lean blow-out

Leading edge

Light source

Mass flow controller

Near-ultraviolet

Parabolic mirror

Parts per million by volume, dry

Standard cubic feet per hour (gas at $14.7\ psia$ and $70^o F$)

Standard cubic feet per minute (gas at $14.7\ psia$ and $70^o F$)

Standard liter per minute (gas at $14.7\ psia$ and $70^o\ F$)

Ultraviolet

Acknowledgements

Abstract of the thesis

Flame Characterization and NOx Emissions Prediction for Reactions Generated by

Aeroengine-Derived Lean Direct Injectors, Operated on Hydrogen and

Hydrogen/Natural Gas Blends

by

Iker Gomez Escudero

Master of Science in Mechanical and Aerospace Engineering

University of California, Irvine, 2023

Professor Jack Brouwer, Chair

A set of 16 aeroengine micromixing injectors was adapted from a lean direct injection of fuel concept to be operated on hydrogen or hydrogen / natural gas blends.

A statistically designed test plan was first employed to evaluate the lean blow-out limits of the test hardware, depending on the preheat temperature of the air flow, the air pressure drop across the airbox, and the fuel composition. This resulted in some clear trends in injector stability as a function of not only the combustion conditions, but also injector geometry.

Fuel composition was the main factor influencing lean stability limits. The combustion conditions with a higher hydrogen content were those with a wider range of stability, because of the higher reactivity and diffusivity. On the injector geometry factors, both low levels of air split and air swirl expanded the lower flammability limits.

A second statistical test plan was designed adding the adiabatic flame temperature as a fourth factor. Emissions and flame diagnostics were evaluated simultaneously.

Regarding flame structure characterization, three different cameras were operated in parallel. A Nikon D90 was used to capture the visible spectrum of the flame, an FB-N9-U Dynacolor camera to record the OH* chemiluminescence, and a Phantom v7.1 to record the high-speed dynamics of the flame.

The current thesis focused on the responses extracted from the OH* chemiluminescence imaging. Because of its direct correlation with the rate of heat release, OH* is commonly used to characterize the flame front. These responses were, for the most part, the flame area and its average brightness, the heat release area and its center of gravity and leading edge. An analysis of variance was performed for each response, with significant indicators of p-values lower than 0.05.

The effect of the confinement ratio of the flame by the combustor quartz tube was also studied, since its dimensions were arbitrarily defined during the design of the setup. A reduction in its length and diameter concluded that no significant change occurred on the flame structure because of it.

Finally, the thesis concludes with connecting the NOx emissions and the imaging flame character-ization. A Random Forest machine learning algorithm was generated, yielding into 80%-accurate predictions of the NOx emissions as a function of injector geometry, combustion conditions and OH* chemiluminescence responses.

Part 1

Introduction

Gas turbine power plants are one of the most energy-consuming sectors [1]. As a result, they are targets for decarbonization through the use of low carbon fuels. [2]

The decarbonization of gas turbines through the use of renewably generated hydrogen as an alternative to natural gas is one possible approach. However, some significant differences between these fuels need to be addressed and further studied to allow such a transition. One of the main obstacles to the introduction of hydrogen into conventional applications is the polluting NOx emissions. Premixed systems are currently used to reduce them, but this comes with a second drawback or concern, the risk of flashback harshly damaging the hardware[3]. As an alternative, the lean direct injection approach strives to obtain a premixed-like condition that minimizes the premixing time and therefore prevents flashback.

Hydrogen has higher flame speeds than natural gas. By increasing the flame speed, the flame moves upstream and the risk of flashback increases, meaning that it enters back into the nozzle. Since this component is not designed for such increments of temperature and pressure, they can be severely damaged. The second drawback comes from hydrogen's higher adiabatic flame temperatures compared to natural gas, if the fuel-to-air ratio is kept constant. In addition to the mechanical effects on the turbine components, this critically affects the thermal NOx formation, which comes mainly from the Zeldovich mechanism on gas turbines (a process accelerated exponentially with temperature). For gas turbines, a way to address this issue may come with leaner combustions when operating on hydrogen.

The literature presents several studies focused on the combustion characteristics, flame structure, combustion instabilities, and emissions of gas turbines operated on hydrogen, or hydrogen blends. Burning lean and uniformly-mixed could minimize the temperature-sensitive formation of the so-called thermal NOx by reducing the peak combustion temperature. An effective way to enhance this fuel transition can also be linked to the use of micromixer combustors, which attempt to produce smaller, thinner, or more compact flames that minimize the residence time at high temperatures of the fuel mixture. Other alternatives are multi-point injection or burning regions [4].

Micro-mixing technologies have been the focus of companies such as Parker Hannifin, Honeywell, General Electric, and Mitsubishi, among others. It reduces the spatial scale of the air and fuel mixture, and therefore the residence time for the products and the associated risk of autoignition. Rather than creating a single, uniform flame, micromixer combustions are characterized by a series of multiple, smaller flames with short residence times. They are typically modular, so they can be scaled and

combined to achieve the desired performance.

Several studies have used digital imaging techniques to characterize and monitor combustion flames, so as to assess the flame stability, visualize the non-visible spectrum, etc. Even though hydrogen flames might be visible to the human eye [5], with examples as the NASA Glenn hydrogen burner [6] and NASA's shuttle [7], because of its dim visible spectrum the interest has been more focused in flame spectroscopy. OH*, CH* and C_2* chemiluminescence, among others, have been used as passive diagnostics, being related to the heat release rate, flame structure and reaction rate [5] due to its origin in exothermic chemical reactions [8]. To capture the UV OH* chemiluminescence, ICCD (intensified charge-coupled device) cameras are used, because of the potential that the intensifier sensors provided. However, the main drawback is the high cost associated with these. For this reason, several studies have been working towards cheaper alternatives to register the UV spectrum in which OH * occurs, as [9].

This thesis focuses on the atmospheric evaluation of the injector performance. Collins Aerospace designed and provided a total of 16 injectors, constructed using additive manufacturing. They were engineered seeking to keep both the air and fuel effective areas constant, mapping a design space based on the following three main factors from their geometry:

- Air split: ratio between the inner and outer flows of air.

- Fuel swirl: inclination with respect to the verticality of the fuel passages.

- Air swirl: inclination with respect to the verticality of the inner-air passages.

Table 1 summarizes such details, while Figure 1 depicts the injector design.

From the overall study of the injectors' performance, the current thesis focuses on the following goals:

1. Assessment of the lean blow-out limits of the different injectors operating under a range of combustion conditions, and their effect on the injector performance.

    (a) Can the supplied injectors operate on 100% hydrogen fuels?

    (b) How does the injector geometry affect the stability of the combustion?

    (c) How do the operating conditions affect the stability of the combustion?

    (d) Can a model be extracted to explain or predict stability behavior based on testing factors? How is the stability affecting the injector's performance?

2. Characterization of the reaction flames by means of different imaging techniques.

    (a) Find an imaging technique that can be used to record the wide variability of flames that result from the testing design.

Table 1: Injectors configuration.

Configuration	Air Split	Fuel Swirl	Air Swirl	Air Effective Area [in2]	Fuel Effective Area [in2]
1	0	-1	-1	0.1512	0.0070
2	-1	0	1	0.1485	0.0062
3	0	0	0	0.1458	0.0061
4	0	-1	1	0.1497	0.0062
5	-1	-1	0	0.1474	0.0067
6	1	1	0	0.1465	0.0049
7	1	0	1	0.1538	0.0062
8	0	1	-1	0.1550	0.0050
9	1	0	-1	0.1525	0.0062
10	0	1	1	0.1494	0.0052
11	-1	1	0	0.1429	0.0050
12	-1	0	-1	0.1485	0.0061
13	1	-1	0	0.1489	0.0071
14	1	1	1	0.1524	0.0051
15	1	1	-1	0.1484	0.0052
16	-1	1	1	0.1456	0.0052

    (b) Determine representative imaging responses to characterize the flames.

    (c) What are the factors that affect the selected imaging responses and how do they do it?

3. Is it possible to predict the NOx emissions based on the injector factors and their LBO stability, the operating conditions and the imaging study of the flames?

    (a) What are the most relevant imaging responses to this correlation?

The following tasks were implemented to answer the research questions:

- Task 1: Design the test rig setup

- Task 2: Design the imaging diagnostics setup

- Task 3: Construct the test matrices

- Task 4: Gather all the experimental data

- Task 5: Analyze the experimental data

(a) Upstream view of the injector design.

(b) Cross section view of the liquid injector from which the gas injector was derived.
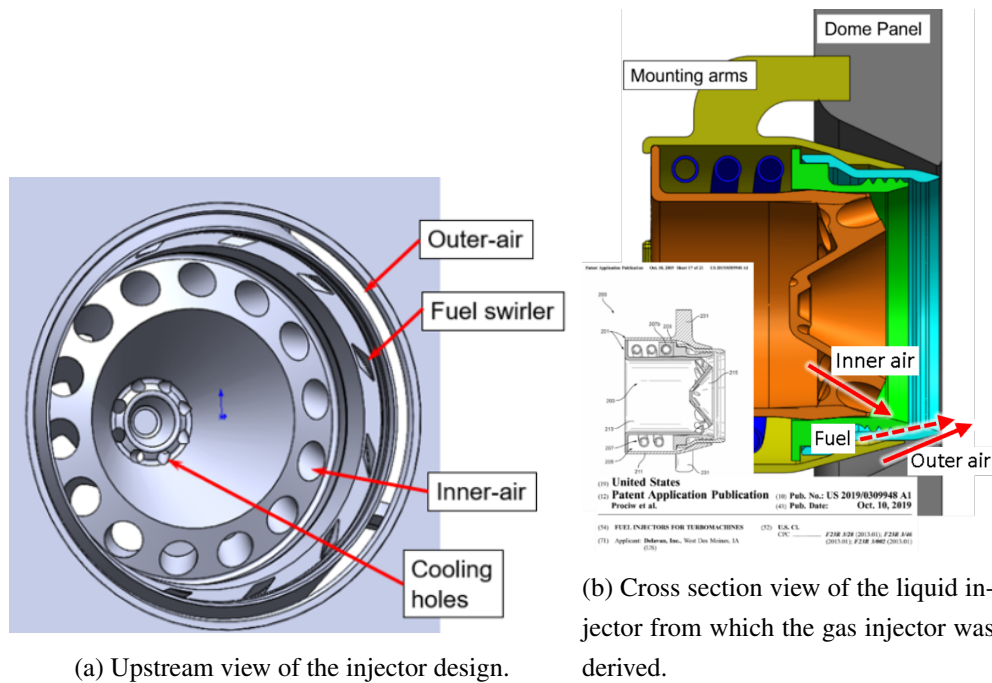
Figure 1: Injector design. As a reference dimension, the injector's diameter is about 1 inch.

Part 2

Background

In this part of the thesis, an introduction to the use of hydrogen in gas turbines is provided. Then, because a key strategy to attain low emissions performance is operating lean, flame stability and lean blow-out limits are discussed.

As the thesis emphasizes imaging methods, a review of possible techniques is presented and the methods adopted for use are highlighted.

Regarding the post-processing of imaging results, strategies for extracting information of interest from the images are reviewed. Finally, analysis methods for interpreting and quantifying information of interest from the images are reviewed, including both statistically based methods (e.g., analysis of variance) and machine learning models. The overall context for the analysis approach is the goal to connect convenient imaging methods to other performance aspects of the combustion system such as stability and/or emissions performance.

2.1   Hydrogen combustion in gas turbines

Gas turbines (GTs) are used to generate electricity due to their high power density, rapid start-up process, and feasibility in combination with other power generation units [10]. GTs' performance mainly depends on the combustion procedure, which is influenced by the fuel used. The majority of current GT-based power plants use fossil fuels [11]. As a result, despite the benefits of GTs for power generation, a focus on decarbonization is needed for these devices to provide benefits in the future.

On the basis of this fact, a cleaner fuel source should be considered to be used. Hydrogen, based on a mass energy density, represents a huge improvement even compared to conventional fossil fuels and even more so considering its low emission of noxious gases.

Some efforts are currently being made on this line, studying, for instance, lean-premixed pure hydrogen combustion, and more importantly, the avoidance of the associated drawbacks of flame flashback, NOx emissions, etc. [12] Considering the natural gas turbines as the basis of the study, hydrogen-fueled GTs may require some modifications to prevent these issues, such as the nozzle architecture that is now seeking small-scale multi-injection structures, and axial fuel staging technologies to fight against elevated flame temperature and residence times to reduce nitrogen oxide emissions.

However, based on [13] and [14], no major structural changes are required with respect to natural gas turbines. Compressor, turbine, and other components could just suffer minor modifications, whereas the fuel supply line might be increased because of the much lower density of hydrogen.

Other studies on the main topic of hydrogen-fueled micro-mixing injection turbines, such as [15] and [16], have also analyzed these trade-offs. The latter, by means of the use of OH* chemiluminescense for flame characterization, pointed out the aforementioned reduction of thermal NOx by "burning lean and uniformly mixed fuel-air mixtures to reduce peak combustion temperatures" ([16] page 2), which indeed produced small, thin and compact flames, thus reducing the high temperatures and residence time. Refer to section 2.4 for more details on the different techniques used for flame characterization, due to the reduced visibility of hydrogen flames.

Thus, hydrogen-containing fuels such as mixtures of hydrogen and natural gas (methane, basically) could result in great benefits for gas turbine use, such as reduction of NO and CO emissions or extension of stability limits and decrease of NOx emission [10]. However, a series of challenges must be faced to meet the levels of NOx emissions that are imposed, as well as the stability and blowoff limits that hydrogen flames entail, or the demand to avoid flashback.

2.2 Flame stability

Flame stability plays an important role in low NOx combustion processes when operating under very lean conditions. Its mechanism is driven by the local speed of the flame and the local inlet flow velocity, including three mechanisms of flame stability: the attached flame on the burner, the lifted base of the flame from the burner, and the extinction of the flame as a flame elevated or an attached flame [17].

For a flame speed greater than the inlet fuel flow, the flame moves back causing flashback, but if it is too small the flame could reach the LBO limits (see section 2.3) [18].

Flame stability is typically linked to the following three parameters: the liftoff height, the vertical distance at which the flame is located above the burner because of the high jet velocity. Second, the liftoff velocity, defined as the inlet flow velocity at which the flame is lifted over the burner. Finally, the blow-out velocity is such that the combustion cannot be supported and the flame is extinguished. [19] It is worth mentioning the difference between blow-out and blow-off here, since it it linked to the previously introduced concept of lift-off: the blow-out condition is that in which the flame is extinguished because the combustion cannot be held anymore, while the blow-off is referred to the specific case in which the flame is extinguished being lifted above the burner.

Regarding the flame stabilization modes, they are typically classified into three types as well: premixed flame propagation models, in which the premixing situation ahead of the flame front of a lifted flame is taken into account; the laminar flamelet models, which regards the flame lift-off because of laminar flamelets quenching; and the large-scale turbulent structural mixing models that consider that the flame lift-off occurs because of the flame extinction due to large-scale, turbulent structures. [17]

Wu et al. [17] performed several stability tests to compare pure hydrogen, hydrogen-methane, and hydrogen-propane flames. For the $H_2 - CH_4$ mixture, it was shown that for more than 40% methane the flame remained attached until it extinguished, but if less methane was used, the flame lifted up before blowing off; in terms of stability, it depended on the concentration of each component.

For pure hydrogen flames, the liftoff velocity was found to be 730 m/s, and the liftoff height linearly increased with this velocity.

According to [20], Wu et al. concluded that the addition of hydrogen induced an increase in the lean stability limit. Schefer [20] determined that adding up to 20% of H_2 resulted in an increase of about 15%. More details can be found in the following section.

2.3   Lean blow-out limits

The equivalence ratio ϕ is defined by the fuel-to-air (FAR) ratio used in the combustion, over the stoichiometric fuel-to-air ratio, as shown in Equation 1. Therefore, ϕ equal to 1 means that combustion takes place under stoichiometric conditions, greater than 1 means a fuel-rich combustion (i.e. more fuel than the stoichiometric proportion) and less than 1 means a lean combustion (i.e. less fuel than the stoichiometric proportion).

$$\phi = \frac{FAR}{FAR_{stoich}} = \frac{F/A}{(F/A)_{stoich}} \tag{1}$$

For the sought purposes, the lean conditions are tested: burning less fuel than stoichiometric, to reduce the consumption and emissions. More specifically, when testing lean blowout limits, the leanest condition is sought. The lean blow-out (LBO) represents the leanest equivalence ratio at which the flame can be sustained before extinction.

Ultra-lean combustion, with proper homogeneous fuel-air mixing, yields a reduction in flame temperature, which, indeed, minimizes NOx formation [21]. Then, in order to obtain lower emissions, the flame stability must be ensured under lean conditions.

The addition of hydrogen to hydrocarbon fuels has been proven to be a feasible method to increase the LBO limits. Schefer R.W. et al. [20] and [22] showed a reduction of the lean stability limit of 10.4% and 16.6% for the introduction of hydrogen 10% and 20% into methane / air flames, respectively. Wicksall D.M. et al., [23] and [24], on the other hand, compared pure methane flames and 60% methane and 40% hydrogen (in volume), to observe that the flame and flow structures were different: the location of flame stabilization was modified by hydrogen, the flame being shorter and more robust. Nguyen and Samuelsen [25] also concluded that hydrogen addition could broaden the lean stability limits, while Jackson et al. [26] concluded that these improvements were mainly attributed to increase in flame speed. Ren et al. [27] showed that an addition of a 8% hydrogen increases the laminar flame speed between 5 and 10%, according to their computation predictions estimating a 7%.

Guo et al. [28] went into detail with respect to emissions. Despite the increase in NO emissions for a given ϕ by adding hydrogen, as ultra-lean conditions can be operated due to this additional H_2 there are significant reductions in NOx emissions.

If pure, ultra-lean hydrogen-air premixed flames are studied, as Vance et al. did in [29], it is observed that H_2 flames stabilize beyond the lean flammability limits due to their stronger preferential diffusion effects. Referring to Figures 2 and 9, in which the experimental and simulated radiation intensities are observed for different equivalence ratios, they concluded that the extinction neck happened because of an unrestrained stretch rate, and also that residual flames were present after the extinction of this neck.

7

On their experiments, they found some spherical flames under further lean conditions, while further numerical modeling was required to better capture this phenomenon.

2.4 Imaging diagnostics

2.4.1 Schlieren and shadowgraph techniques

Non, or low visibility of hydrogen flames makes one think about using techniques such as schlieren or shadowgraph. They rely on image refractive interferences in the transparent medium, as stated in [30], because of the density gradients ($\partial n/\partial x$ and $\partial n/\partial y$) caused by the flame in this case. According to Gladstone-Dale law, the density of the fluid ρ and its refractive index n are correlated as follows, where k is a constant for the working fluid:

$$n - 1 = k\rho \tag{2}$$

Even though schlieren and shadowgraph techniques are almost identical, the main difference is that the former is sensitive to the first derivative or gradient in density, while the latter is sensitive to the second derivative. This makes the latter a bit simpler, even its later development. In terms of the required instruments, both look almost the same too (see Figure 1 from [30]), but Schlieren incorporates a knife edge that intensifies the visibility of those gradients by blocking part of the light, thus reducing the brightness of the resulting spectrum. [30] The knife edge intensifies the sharpness of the boundary between blocked and unblocked rays.

BOS, or background-oriented schlieren (also known as synthetic schlieren), is preferred to shadowgraphy when flows have weak gradients, one wants to perform a quantitative work, and large natural backgrounds are available. On the other hand, shadowgraphy outperforms when detecting shock waves and thermal turbulence, and for real-time displays without delays due to the computer processing. Thus, schlieren is sought in this project.

As shown in Figure 2, the most typical z-type schlieren configuration, it is formed by the light source (LS), which could be a LED source to narrow the used beam; two parabolic mirrors, PM1 collimating the bright from the LS into the focus from the second lens PM2, after crossing the phenomena of study (S); the previously mentioned sharp knife edge (KE) at the focus of the second lens, and finally the camera (C).

Figure 3a and Figure 3b show two different light sources used for an equivalent flame, with a z-type schlieren setup: the first was taken with a white light source, while the latter was using a high-power LED source.

In both cases, a simple flame was recorded: a canned wick was lit and placed on an optical table, as described in Figure 2, in order to obtain some preliminary schlieren images. However, as detailed in

8
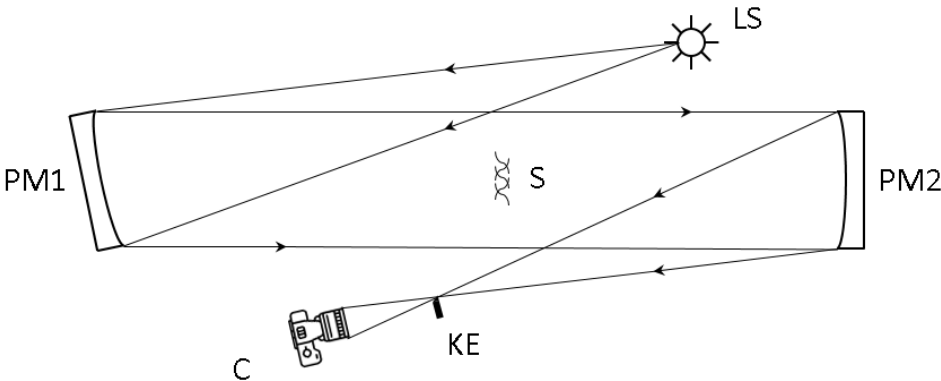
Figure 2: Z-type schlieren system.

the following sections, this project was designed to hold the flame in a round cylinder, not open to the atmosphere, which implies some issues for this phenomena.
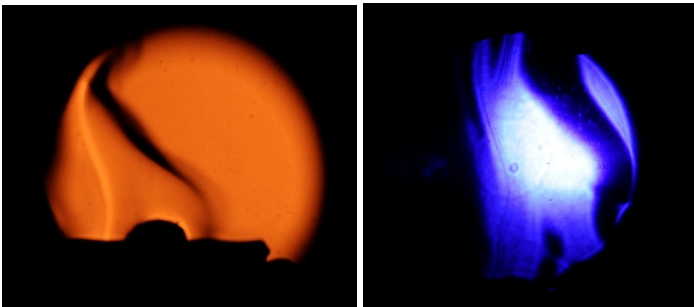
(a) Using a white light source.   (b) Using a LED source.

Figure 3: Schlieren images of a flame.

When dealing with round surfaces, not simple flat windows or even an open atmosphere environment, the cylinder is also acting as a lens, causing the collimated beam to diverge [31] (see Figure 4a), so the Schlieren effect would no longer be visible. As cited in the cited article, the problem can be compensated by imposing a divergent effect with positive refractive power surfaces, as sketched in Figure 4b.

Implementing these correction lenses implies a design and optimization process out of the scope of the current project, even more considering the recent initialization of it and the uncertainties linked to the hardware: once everything is fixed and works as expected, this could be implemented if convenient. As an alternative, the schlieren technique is set to be used with rectangular windows instead: the combustor-holding plate is designed so that it can mount either round cylinders (two different diameters) or rectangular windows forming a square shape, as shown in Figure 5.

Being one of the goals of the project, the study of the blow-out of the different configurations, as well

(a) Collimated beam passing through a cylinder.

(b) Correction lenses.
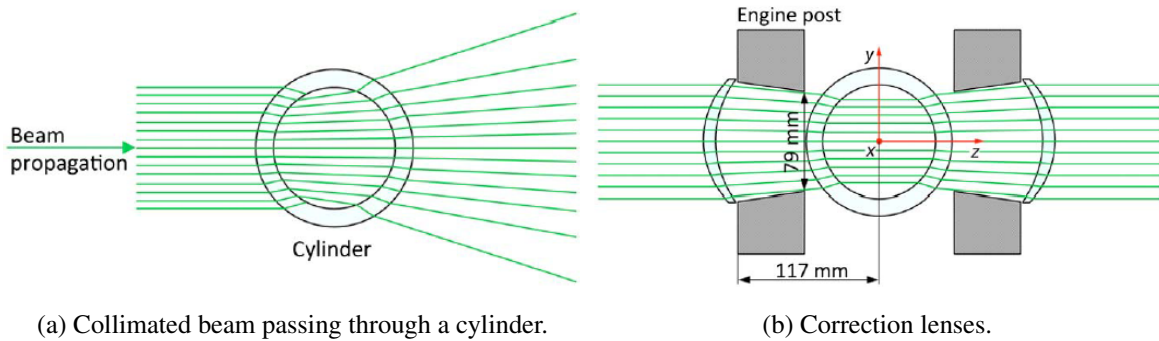
Figure 4: Schlieren images in round cylinders. [31]
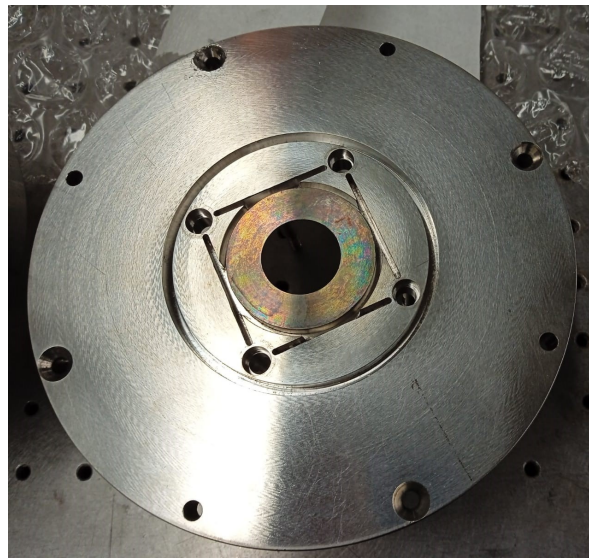
Figure 5: Combustor-holding plate.

as the characterization of the flame structure, the confinement ratio plays an important role on it, as proven in [32]. They showed that the lean blow-out limit decreases by increasing the confinement, thus indicating a better stabilization performance: bigger chambers were observed to enhance the resistance to the stretch-induced extinction.

Because of the change in geometry in order to incorporate the flat windows for the schlieren purposes, an extra cylinder diameter is also considered to be tested in order to get a more detailed study of the confinement ratio effect. Thus, two different areas (between both cylinders) and two different geometries with the same areas (smaller cylinder and squared shape) are planned to be tested. For the round cylinders, however, the schlieren technique will not be used because of limitations with the optical access.

2.4.2   OH* chemiluminescence

Hydrogen flames are not invisible, but weaker than typical hydrocarbon flames [5]. These have shown reduced light levels, so not just the visible spectra but also the ultraviolet flame emissions are commonly used on their analysis: OH*, CH* and C_2* chemiluminescence are often used as a passive diagnostic related to heat release, flame structure and reaction rate.

As stated in the cited article, the blue emission from these hydrogen flames corresponds to the superimposition of structured emissions and broadband continuous emissions.

Figure 5a in [5] shows the relevance of OH* chemiluminescence emissions on hydrogen-air flames, with an ultra-violet wavelength of around 308 nm, as well as the vibration excitation of water molecules, in the infrared band.

Due to the relevance of OH* emissions, they are set to be studied within this project, as [8] did. In the cited article, OH * and CH * chemiluminescence was used to control premixed flames, by means of a correlation between OH* emissions and the equivalence ratio ϕ, the heat release rate, and the adiabatic flame temperature. Figure 6 reflects the increasing trends of OH* with an increasing equivalence ratio. The OH* can be correlated to the adiabatic flame temperature, since the latter is computed using the equivalence ratio. For a given air flow, the equivalence ratio determines the fuel flow (the higher the equivalence ratio, the higher the fuel flow), according to Equation 1. See [33] for a more detailed experimental study of the effect of the equivalence ratio on OH* chemiluminescence.

Chemiluminescence refers to the process by which specific molecules are lifted to an excited state (the * symbol stands for the electronic excited state) by exothermic reactions, and then evolve to equilibrium energy levels when a photon is emitted [8]. Because chemiluminescence is formed by the exothermic reactions of combustion, it marks the temporal location of the originating reactions. These emissions also provide information about the fuel/air reactions, by means of the responsible molecules of the chemiluminescence (OH*, CH*, C_2*...) [34].

A commonly used approach to capture these emissions is by using an oscilloscope, by converting the UV light into electrical signals and then visualizing them as waves on the oscilloscope screen. However, the present study is inspired by [9] to capture the ultraviolet (UV) radiation with devices as simple as possible. ICCD (Intensified Charge-Couple Device) cameras are a powerful tool to capture OH* chemiluminescence emissions, by picking up and amplifying weak OH * signals with the image intensifier and capturing the amplified light signal as an image with the image sensor. On the other hand, simpler solutions such as smartphones were shown capable of detecting UV radiation in the broadband between 200 and 370 nm, with the UV photodiode, UVM-30A, Guangzhoy Logoele Electronics Technology sensor (as mentioned in the cited article). It has also been proven that CMOS sensors are able to detect this radiation [35].
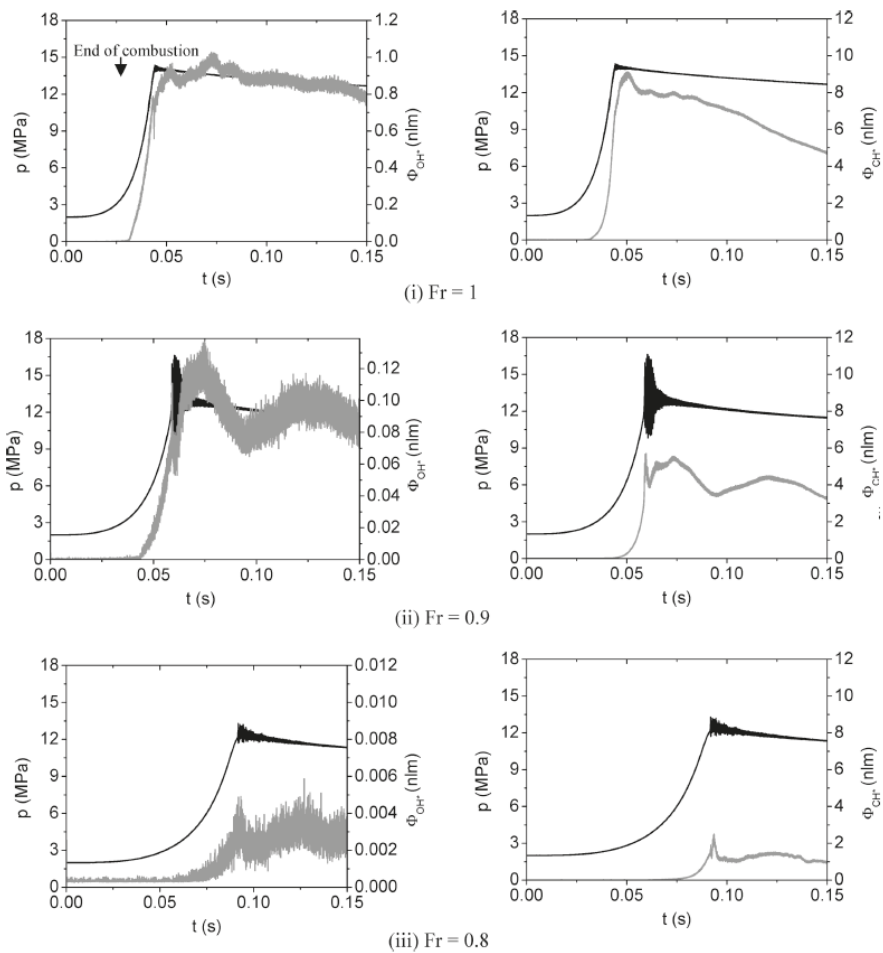
Figure 6: "Temporal evolution of the pressure (black line) and OH* (gray line in the left plots) and CH* (gray line in the right plots) chemiluminescence in *n*-heptane premixed combustions with autoignition for different equivalence ratios, with a fixed initial pressure and temperature of 2.0 MPa and 443 K, respectively." [8]

It seems reasonable, thus, to use low-cost smartphone sensors for UV detection, although the problem arises in the use of specialized filters, which drastically increase the cost (up to a few thousand dollars). A cheap alternative is proposed in [36], in which a PiCam lens and filter (originally absorbing the UV signal) are manipulated to develop a UV camera (ranging in the order of a few hundred dollars). Both the improvement and enhancement of the UV sensor are used in the 200 to 400 nm wavelength range, as stated in [37], to allow the photons detection in this near-UV (NUV) range. NUV digital imaging is problematic, since conventional CCDs and CMOS detectors have limited responses in this band, whereas commercial digital cameras present UV blocking layers in sensor windows: no UV blocking filter CCD or CMOS sensor, and a filter to block all except NUV radiation could be the solution [38].

Sony's IMX487 sensor (see [39] for more details) offers a promising relative quantum efficiency curve, for the wavelength range of interest. It is a CMOS UV waveband sensor, from Sony Semiconductor Solutions Corporation, that could work for the sought OH* chemiluminescence emissions capturing. It is a new model, so it is rarely found in commercial cameras; after some research, the Dynacolor USB3 Vision Camera, FB-N9-U model (see [40] for more details) has been found to mount it. The UV camera datasheet shows a relative response larger than 0.7 for the wavelength of interest, 308 nm, which means that it could be used to detect the OH* chemiluminescence.

This would mean a significant cost reduction from the iStar Andor camera, previously used by the laboratory group to capture the OH* emissions (see more details in [41]).

2.4.3   OH* chemiluminescence and NOx emissions

The greatest contribution to NOx emissions from gas turbines comes from thermal NO, which is generated in the post-flame area at temperatures above 1800 K [42]. As detailed in [43], the limiting reaction of such mechanism is affected by temperature, and has a high activation energy. Due to this linkage between NO formation and temperature, controlling the latter is an effective way to restrict NOx emissions. Additionally, the prompt NO pathway also plays an important role in hydrocarbon flames.

As has been previously introduced, OH* chemiluminescence is generated by the transition of excited radicals. These are involved in the production and consumption reactions of NO [44], so they can be linked. Additionally, OH* chemiluminescence is also related to the rate of heat release, and since temperature is a decisive factor in NO formation, a linkage between NO formation and chemiluminescence must exist.

Several studies have compared NOx emissions based on NO* and OH* chemiluminescence, among others, like Wang et al. [45] and Liu et al. [43]. The latter proposed an experimental relationship between NOx emissions and CH* and OH* chemiluminescence:

$$C_{NO_x} = 16.64 OI_{CH*,m} - 3.26 \tag{3}$$

$$C_{NO_x} = 22.90 OI_{OH*,m} - 10.62 \tag{4}$$

where OI_m stands for the normalized overall intensity (ranging from 0 to 1) and C_{NO_x} was measured in ppm corrected at $15\% O_2$.

Therefore, it has been proved that OH* chemiluminescence is directly related to NOx emissions, following an increasing linear trend.

2.4.4 High speed imaging

Many combustion research projects use high frame rate imaging for diagnostics, such as [46] in which a high-speed video camera was used to detect the luminosity of the natural flame for the studies of flat walls impinging spray flames.

High-speed imaging is used for mixing processes, flame stabilization, and ignition, among others, as described in the review paper [47], by recording chemiluminescence emissions, schlieren or shadowgraphy images fluorescence, etc.

The nonlinearities of combustion that cause the peculiar evolution of a flame, the mixing process, or the ignition and extinction of a flame are processes in which high-speed imaging is required to capture their nature. Therefore, it is the stability study of a flame, and high-speed video cameras play an important role in this project.

Digital cameras employed in this mode allow one to capture transient processes with very short time scales, allowing the opportunity to use very high frame rates to understand detailed combustion aspects. The cited review [47], discusses some limitations regarding the maximum frame rate, minimum pulse energy, and pulse repetition rate, according to the instrument used and the phenomena studied.

In the present study, the aforementioned iStar Andor camera, and possible the GB-N9-U Dynacolor camera, are used in a high frame rate to capture these high-speed phenomena for the later imaging diagnostics.

2.4.5 Flame characterization through digital imaging

Digital imaging is an effective way for flame stability monitoring and characterization: a camera captures the intensities of each pixel, the geometric, luminous and thermodynamic parameters are computed, and the flame stability is assessed [48]. There are different ways to do so: using chemiluminescence radicals; studying lift-off height, length and emission levels; using direct imaging for 2D and 3D flame monitoring; among others, where the ultimate goal is to measure and quantify the relevant features of a flame (size, shape, brightness...), and then assess the stability through the statistical analysis of them.

Some geometric and luminous parameters, such the ignition points, the luminous region, brightness and non-uniformity, are found using digital image processing techniques; geometric and luminous instabilities are computed with the statistical analysis of the previous; the oscillation frequency is also derived from the intensity signals; and the temperature distribution can also be measured with a two-color method, according to [48].

Based on [49], the following parameters are defined.

- **Geometric parameters**. Ignition points (I_p in Figure 7) represent the distance between the burner and the flame ignition, and they should be steady for a stable flame. Each I_p is found by looking for the illuminating point over the flame root. The ignition area (A_{ip}) is the area between the burner outlet and the ignition points, normalized to the area of the entire field of view. It gives information about the flame ignitability. Finally, the spreading angle (α_s) is formed between the straight lines limited by the outer edges of the flame.
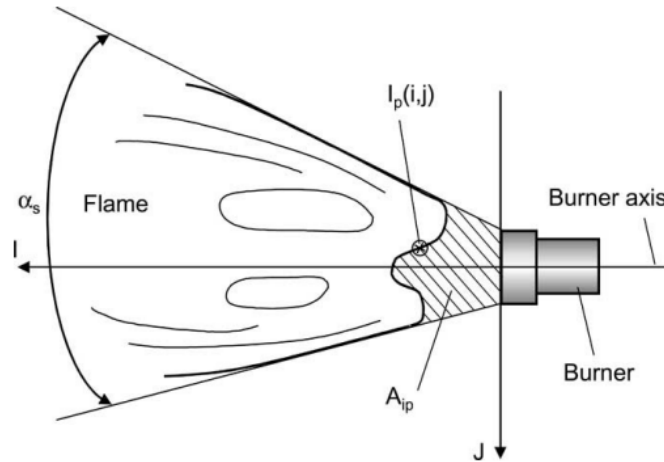
Figure 7: Flame geometric parameters. [49]

- **Luminous parameters**. The brightness is given by the average gray-level of the luminous region of the flame (according to [50], the cross-section area occupied by the flame, normalized to the entire field of view), normalized to the full-scale gray-level, while the nonuniformity is computed as the mean deviation of the gray-levels of each pixel over the luminous region

- **Thermodynamic parameters**. The temperature can be measured by means of a two-color pyrometry, based on the emissivity associated with temperature radiation; see also [51] for more details. Finally, they define the flicker as "the dynamic alternating components (ACs) superimposed on the steady state (DC) or brightness level of the flame" ([49] page 3)).

Other factors as the flame length and width have been widely used when characterizing flames, as well as the color pattern and other various features [52].

2.4.6 Image recognition and machine learning algorithms

An automatic process for image classification might be based on image recognition. It can be found in many industries and processes, such as defect identification, medical imaging, etc., and it is based on the identification of objects or features in images or videos. It relies on deep, machine learning algorithms trained on the training data set (with their associated categories) and then implemented

into the test data.

Matlab, the software to be used for the imaging post-processing in the current work, has some built-in features that allow such a process [53], based on some image labeling apps like the one explained in [54], or based on deep learning and machine learning algorithms.

Because of the already created machine learning libraries that Python has, it is a commonly used language to implement machine learning algorithms. Based on the applications for the current work, below is a brief introduction to some machine learning algorithms that could be considered:

- **Deep Artificial Neural Network**, or Deep ANN: a deep ANN is an artificial neural network with various hidden layers between the input and output layers. ANNs were originally inspired by models of brain processing, simulating a model of neurons to learn from training data. It consists of a series of units that receive input information from the previous layer, weigh each of them, and add them all together to construct the output for the following layer. By means of some activation functions, the amplitude of the output is regulated. [55] [56]

- **Random Forest**: a random forest algorithm is a combination of decision trees, each depending on a series of random variables. These trees are a binary recursive partitioning of the sample space, and the succession of decisions made by each stage produces the final prediction based on the inputs. [57] [58]

- **AdaBoost**, or Adaptative Boosting: AdaBoost was the first functional implementation of the boosting techniques in machine learning. These are intended to create accurate predictions by integrating various less accurate algorithms or rules. [56]

- **Support Vector Machine**, or SVM: it is a supervised algorithm (i.e., the available data is labeled containing the features or factors and the corresponding label or category) that builds a model to assigns to the new data one of the different categories in which the training data set was divided, dividing the data space by maximizing the gap between classes. [59]

2.5   Takeaways from the literature review

The decarbonization of gas turbines has aimed towards the use of hydrogen as fuel. However, compared to commonly used natural gas fuels, certain drawbacks regarding its stability and possible issues with flashback phenomena should be considered. Pre-mixed systems are currently used to obtain low emissions, but they inherently increase the risk of flashback. To simulate the preferred conditions of a premixed combustion, but to reduce this risk, lean direct injection has been studied. For the lean direct injectors to be used, the lean stability must be characterized as a function of the injector geometry parameters and the operating conditions.

Because of the dim visible spectrum that hydrogen flames present, the studies in the literature typically use the OH* chemiluminescence emissions to characterize the flame front, locate the temporal origin of such reactions, etc. Therefore, the UV spectrum is set to be studied deeply on this project, in order to characterize the reactions of the set of injectors. A proper imaging technique was required to capture the combustion phenomena occurring under various operating conditions. Once the techniques are selected, the captured images need to be processed to extract the meaningful information: therefore, there is a clear need to properly define the representative imaging characteristics. Then, these imaging responses need to be analyzed to describe how they are influenced by the design factors, so as to explain the resulting flames with the controlled variables.

The imaging characterization of these flames is meant to be correlated with NOx recordings, in order to further study the effect of micromixing technologies on such emissions. The overall idea is that this concept creates more compact flames, therefore reducing the residence time at high temperatures of the reaction products. Furthermore, the ability of hydrogen to stabilize reactions at very lean mixtures could allow the reaction to be operated at lower adiabatic flame temperatures and therefore decrease the thermal NOx mechanism. Several studies have stated that there is a direct correlation between NOx emissions and (OH*) chemiluminescence, and therefore, the question of a feasible way to predict NOx is open, based on the imaging characterization of the combustion.

Part 3

Approach

The ultimate goal of the thesis is to find the best performing injector to be used in an industrial engine gas turbine, based on an aeroengine-derived lean direct injector. The lean direct injection approach was implemented to mimic the premixed conditions that favor the NOx emission reduction, but limiting the risk of flashback. Because of this stability criteria, the set of hardware needs to be assessed in terms of its LBO limits. The experimental rig and corresponding test matrix have to be addressed first.

Due to the various scenarios to be assessed, especially the main differences between hydrogen and natural gas combustion flames, the proper imaging diagnostics tools need to be selected and configured on the optical tables. Once the setup is implemented, all the performance data can be collected from the experimental testing, and further post-processed so as to obtain the representing models.

For this overarching goal of linking imaging diagnostics with injector performance, during atmospheric testing screening, the following tasks were completed:

- Task 1: Design the test rig setup

The experimental test rig was composed by the combustion apparatus itself, and also the data logging devices that were used to characterize each testing condition. The combustor was installed between two optical tables on which the three different cameras were sitting, and it contained an emissions probe right at the exit of the upper plate connected to the gas analyzer. Auxiliary equipment was also mounted around the apparatus. A more detailed picture of the setup of the test rig can be found in section 4.2.

Three different flows were needed to conduct the experiments: air, natural gas, and hydrogen. Before any experiments were performed, these lines needed to be calibrated to obtain the governing equation between the input variable (pressure before the sonic orifice for the air line and percentage of the MFC valve opening for both fuel lines) and the output flow rate.

To do so, different elements were used and compared with each other to validate the curves obtained: a laminar flow element (LFE), a rotometer, and a Gilibrator. More details on each of the flow metering characterizations can be found in section 4.1.

- Task 2: Design the imaging diagnostics setup

Starting with the literature review to assess which type of camera was more suitable to characterize the combustion that was sought here, their distribution on the optical tables was organized so as to allow their corresponding fields of view to capture the reacting flames.

Due to the need to accommodate different cameras simultaneously, a preliminary design was created using computer design tools. Once the decision on the cameras to be used was made, they were finally mounted one next to each other pointing towards the quartz combustor, as their field of view were big enough to capture the flames from their corresponding focal distance. A more visual description of the imaging diagnostics setup can be found in section 4.3.

- Task 3: Construct the test matrices

The statistically-designed test matrices were constructed using Design Expert, based on a Box-Behnken design of experiments model. Two different experiments were conducted here, one to verify the stability limits of the injectors and the other to evaluate the performance.

The first set was formed by three main factors (apart from the geometric parameters of the injector): the pressure drop of the air across the airbox, the preheat temperature of the air, and the fuel composition (natural gas, hydrogen or a 50/50 mix in volume). This resulted in a 15-point matrix for each of the 16 injectors, so a total of 240 test points.

The second set was formed by four main factors (apart from the injector geometric parameters): the same three as the previous set, and the adiabatic flame temperature. This resulted in a 27-point matrix for each of the 16 injectors, so a total of 432 test points.

More details on the designs and both test matrices can be found in section 4.4.

- Task 4: Gather all the experimental data

Using the first test matrix that was described before, the lean blow-out limit for each conditions was recorded as the fuel flow rate at the flame extinction, and then translated in terms of the equivalent ratio and adiabatic flame temperature. The tests were initialized by fixing the air pressure drop with the air flow rate and the preheat temperature with the electric heater; then, the fuel flow was set at a high enough value to obtain a stable combustion, and slowly decreased until the flame blew off.

Regarding the performance testing, the emissions were recorded from the gas analyzer readings, and the three imaging techniques were recorded simultaneously, capturing one frame with the visible-spectrum camera, a frame with the ultra-violet-spectrum camera, and a sequence of frames with the high-speed camera.

A more detailed procedure can be found in section 4.6.

- Task 5: Analyze the experimental data

The statistical study for both experiments was performed using Design Expert. For the lean blow-out study, the analysis of variance resulted in the equation describing the stability response as a function of the significant factors and their interactions. From this, conclusions about how each factor influences

the equivalence ratio or, equivalently, the adiabatic flame temperature at the LBO were extracted.

The imaging diagnostics was performed mainly on the OH* chemiluminescence recording from the performance study. First, each frame was post-processed to obtain the imaging responses of interest to characterize the flame: flame width and height, average brightness of the flame area, location of the heat release area with respect to the injector, etc. Once these responses were obtained for all the test points, an analysis of variance was conducted using Design expert, to find the statistical models that describe each of them as a function of injector parameters and testing conditions.

Finally, the imaging responses and the NOx emissions were coupled to aim the goal of predicting the emissions based on the injector geometry, combustion conditions, and imaging responses.

A more detailed description of each step of the analysis and the main results can be found in section 4.5.

Part 4

Experimental methodology

4.1   Flow metering characterization

4.1.1   Air metering

A flow is considered as choked or critical when the absolute pressure ratio is 0.528, so the downstream pressure is 52.8% of the upstream pressure [60]. By doing so, the air flow velocity is kept constant after the sonic orifice, even though the mass flow rate could keep increasing because of its dependence on the density.

The mass flow rate going through a sonic orifice, then, depends on the velocity, the density, and the orifice dimensions. Thus, a high-accuracy control can be obtained by fixing the diameter of the hole and changing the inlet pressure. Due to the air flow rates requested, an **125 O'Keefe metal orifice air flow** is set to be used for the air metering. According to its manual (see [60]), this 0.125 inches diameter orifice supplies the air flow rates given in Table 2 as a function of the given upstream pressure.

Table 2: 125 O'Keefe metal orifice air flow specifications.

Supply pressure [psig]	1	5	10	15	20	25	30	40	50	60	70	80	90	100
Air flow rate [SCFH]	50.1	108	148	178	210	241	273	337	401	465	531	596	660	729

However, instead of using the linear trend found with the points from Table 2 (without considering the first three points, in which a nonlinear behavior is found because the non-choked conditions), a calibration curve previously found for this orifice is used (Equation 5, where Q stands for volumetric flow rate, and P for pressure).

$$Q_{outlet}\ [SCFM] = 0.2273\ P_{inlet}\ [psig] + 2.8291 \tag{5}$$

In order to control the upstream supply pressure, a **Swagelok valve** is installed before the sonic orifice, followed by a **pressure transducer** (Tek Bar 3120 B) to allow reading (and later recording, if desired) of the adjusted pressure.

However, before using this setup, it needs to be calibrated. To do so, the pressure transducer reading is compared to a mechanical manometer, which is reliable due to previous laboratory experiments that use it: Equation 6 is the calibration curve for the pressure transducer with respect to the dial reading. On the other hand, the sonic orifice is calibrated as a function of the inlet pressure by using a flowmeter: The air line is connected to this element, and it shows the actual air flow rate going through it. This latter calibration is also validated using a pitot probe to measure the velocity at the center of the air line: approximately, this velocity times the cross section of the line is the flow rate. This calibration curve is shown in Equation 7, to go from the expected Q_{outlet} from the previous equation (Equation 5) to the actual flow rate (calibrated using both the flowmeter and the pitot probe).

$$P_{real} \, [psig] = 0.7985 \, P_{transducer} \, [psig] - 2.0076 \tag{6}$$

$$Q_{flowmeter} \, [SCFM] = 0.7862 \, Q_{expected} \, [SCFM] + 0.7843 \tag{7}$$

Then, the procedure to go from the pressure transducer reading to the actual air flow rate, would be:

1. Use Equation 6 to get the real pressure reading.

2. Use Equation 5 to obtain the outlet flow rate from the sonic orifice.

3. Use Equation 7 to obtain the calibrated real flow rate.

The resulting equation from this process was later corroborated with a direct calibration between pressure reading and flow rate, by using a RMC-series Dwyer flowmeter[1] and a M-series Alicat flowmeter[2]. The final calibration curve reads:

$$Q \, [SCFM] = 0.1924 \, P \, [psig] + 2.853 \tag{8}$$

4.1.2 Methane metering

For the fuel metering, a Mass Flow Controller (or MFC) from Brooks Instrument is used; according to the flow rates that are sought, the model 5851i is appropriate (see [61] for more details), and because of the *i* series, the **microprocessor model 0154**, from Brooks Instrument as well, is used for the read out and control (see [62] for more details).

---

[1]RM-series Dwyer flowmeter operating principle: buoyacy. Fluid flow raises a float: the greater the flow, the higher the increase.

[2]Alicat mass flow technology operating principle: laminar differential pressure. According to the manufacturer, the four steps that the device uses to calculate the mass flow rate are: (i) conversion of turbulent into laminar flow, (ii) measurement of pressure drop across the flow channel, (iii) calculation of the volumetric flow rate, and (iv) calculation of the standardized mass flow rate.

The mass flow controller accurately ($\pm 1\%$ full scale) measures and controls the flow of the gas going through it, based on thermal mass flow sensing: a temperature difference ΔT between the downstream and upstream is created using a constant power heat input P, and it is used to determine the gas mass flow m because of their direct proportionality as described on its cited manual:

$$\Delta T = A \cdot P \cdot C_P \cdot m \tag{9}$$

where A is a constant of proportionality, and C_P the specific heat of the gas at constant pressure.

Because of this C_P, property of the used gas, the mass flow controller needs to be calibrated for the ultimate purpose gas: in this case, methane.

Alternatively, if the mass flow controller is operated on a different gas, a scale shift must be used because of the difference in molar specific heat capacities, resulting into an extra $\pm 5\%$ accuracy loss.

In this case, the used **MFC model 5851i** is calibrated for natural gas (methane)[3], and a flowrate of 1.5 SCFM is specified.

Because of the lack of precision showed for flow rates displayed on the microprocessor, a calibration curve is defined between the displayed values and the fuel flow rates measured with a flowmeter (Gilibrator-2 Calibrator, from Sensidyne, with a range between 20 cubic centimeter and 6 liters per minute). This calibrator gives the actual flow rate reading for any gas that is introduced, by measuring the rise speed of a bubble on a known-diameter cylinder.

It was observed that the flowrate readings from the microprocessor were independent on the specified engineering units. The controller allows the user to set the flow units, but the outlet flow was observed to be the same no matter the specification. For this reason, the unit was fixed to be the percentage reading on the microprocessor ($\%_{micro}$), corresponding to the % of the MFC full scale. Thus, the calibration curve for the methane is given by Equation 10.

$$Q_{CH_4} \, [SCFM] = 0.0152 \, \%_{micro} - 0.0063 \tag{10}$$

4.1.3 Hydrogen metering

Equivalent to the methane metering, the hydrogen is controlled by a **MFC model 5851i**, now calibrated for hydrogen and with a specified flowrate of 19.8 SLPM, and the same **microprocessor model 0154**, both from Brooks Instrument. The microprocessor has four different control channels, so each fuel can be controlled independently with their corresponding units, or using its blending mode (detailed in the next section).

---

[3]As specified on its manual, the natural gas is commonly approximated by its major component, methane. In a previous gas composition study developed by the laboratory group, it was found that a 95.8% of the natural gas was methane.

As it was detected with the methane, the microprocessor is not responding to the defined engineering units, so a new calibration curve is obtained for the hydrogen mass flow controller (Equation 11 and Equation 12). Two different mass flow controllers were used to obtain the highest flow rates of hydrogen that were needed: one calibrated for hydrogen with a maximum flow rate of 20 SCFM ($Q_{H_2,1}$) and the second one with a flow rate of 40 SCFM ($Q_{H_2,2}$).

$$Q_{H_2,1} \, [SLPM] = 0.007 \, \%_{micro} \tag{11}$$

$$Q_{H_2,2} \, [SLPM] = 0.0142 \, \%_{micro} + 0.0058 \tag{12}$$

4.1.4 Blending mode

As defined in the microprocessor manual (cited before, [62]), the blending mode allows to link one *slave* channel to another *master* port: the master channel is adjusted as before, so in this case using the percentage calibration curves presented above, and the slave is linked to the previous by means of the blending ratio:

$$Blending \; ratio = \frac{Q_{slave}}{Q_{master}} \tag{13}$$

Then, in order to control the slave channel, one just has to define the percentage with respect to the master that it corresponds to. See the following examples of mixtures and how to set them with the microprocessor:

- 75% $CH_4 - 25\%$ H_2 mixture of 100 SLPM fuel: the hydrogen channel is set as the slave of the methane port, then CH_4 is set to its flow rate of 75 SLPM, and H_2 is defined as a 33.33% blending ratio, which would correspond to 25 SLPM (a third of the 75 SLPM of CH_4).

- 50% $CH_4 - 50\%$ H_2 mixture of 100 SLPM of fuel: the hydrogen channel is set as the slave of the methane port, then CH_4 is set to its flow rate of 50 SLPM, and H_2 is defined as a 100% blending ratio, which would correspond to 50 SLPM (the same as CH_4). Methane could also be defined as the slave of hydrogen and do everything reversely.

- 25% $CH_4 - 75\%$ H_2 mixture of 100 SLPM fuel: the methane channel is set as the slave of the hydrogen port, then H_2 is set to its flow rate of 75 SLPM, and CH_4 is defined as a 33.33% blending ratio, which would correspond to 25 SLPM (a third of the 75 SLPM of H_2).

However, in this case, since each of the two mass flow controllers has its own calibration curve, the percentage displayed on the microprocessor does not correspond to the same flow rate: 50 % in the methane channel corresponds to a flow rate of $0.754 \, SCFM$, while 50 % in the first hydrogen channel corresponds to $0.350 \, SCFM$.

Due to this deviation, to obtain a mixture $50 - 50$ (that is, the same amount of each gas), the H_2 channel is defined as the master and the CH_4 as the slave with a mixing ratio of 47.5 %.

4.1.5 Emissions check

The hydrogen-methane combustion is given by the following stoichiometric reaction,

$$\mathbf{a}CH_4+\mathbf{b}H_2+(\mathbf{2a + 0.5b})(O_2+3.76N_2) \rightarrow \mathbf{a}CO_2+(\mathbf{2a + b})H_2O+(\mathbf{7.52a + 1.88b})N_2 \quad (14)$$
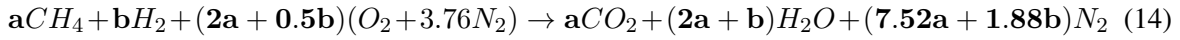
where $\mathbf{a}$ and $\mathbf{b}$ are the stoichiometric coefficients of both fuel components, methane and hydrogen.

Because it is a lean combustion, the fuel is the limiting reactant, so it is used as a calculation basis. On the other hand, as there is an excess of air, some unburnt air will result as a product after the reaction is completed.

This theoretical combustion is used to check the air and fuel metering, as well as the presence of leaks along the lines: in order to consider them as correct, the expected and obtained emissions must be coherent. The Horiba PG 350 gas analyzer is used to characterize the products of combustion: it is placed right after the flame, so it analyzes the gases from the flame.

However, since it only considers the dry products (that is, without water), the products of the stoichiometric reaction are CO_2 and N_2, as well as the excess air components O_2 and N_2.

The gas analyzer allows the user to obtain the fraction of oxygen as a percentage of the analyzed gas, so the expected oxygen excess can also be computed to compare both values and determine the correctness of the system.

By using the fuel flow metering, the fuel molar rates a and b are computed by using the volumetric rate, density and molecular weight,

$$molar\ rate = volumetric\ rate\frac{density}{molecular\ weight} \quad (15)$$

$$[mole/s] = [m^3/s]\frac{[kg/m^3]}{[kg/mole]}$$

and so it is the air flow rate used with the air flow metering. The stoichiometric oxygen flow rate is given by $2a + 0.5b$.

Then, the unburnt oxygen can be easily computed as the difference between the total used oxygen (coming from the air flow rate) and the stoichiometric O_2 ($2a + 0.5b$),

$$excess\ O_2 = total\ O_2 - stoichiometric\ O_2$$

The same procedure applies for the nitrogen excess. Thus, the four expected dry products are determined: stoichiometric CO_2 and N_2, and excesses of O_2 and N_2. So the oxygen excess fraction reads as follows,

$$\%O_2\ excess = \frac{O_{2,excess}}{CO_2 + N_2 + O_{2,excess} + N_{2,excess}} \times 100 \tag{16}$$

Table 3: Emissions check for some burning conditions.

Air [SCFM]	CH$_4$ [SCFM]	H$_2$ [SCFM]	% O$_2$ expected	% O$_2$ measured	% deviation
7.9708	0.4236	0	11.12	11.38	2.37
11.9535	0.6898	0	10.22	10.47	-0.46
11.4340	0.4696	0.4696	11.60	11.91	2.67
10.5682	0.6303	0.6303	6.94	7.14	2.87
10.4913	0	0.6571	18.50	18.57	0.41
13.9930	0	2.1258	14.64	14.92	1.94

Table 3 exemplifies some burning conditions that were executed. It shows a slight misalignment between the expected (from the stoichiometric reaction) and the measured (with the gas analyzer) oxygen emissions: however, as this deviation is less than a 5% in all cases, one can conclude that the system is well calibrated (according to section 4.1) and no significant leaks are found, so it is ready to be used.

The deviation is computed as,

$$\%\ deviation = \frac{measured - expected}{expected} \times 100 \tag{17}$$

The difference between both percentages is linked to different contributions: the air and fuel metering accuracies, the gas analyzer precision, and also the real combustion reaction, mainly. Equation 14 represents the theoretical combustion of methane and hydrogen; however, in reality there are other products as CO, NO, NOx... which should also be considered into Equation 16.

4.2 Test rig setup

The experimental setup is basically formed by the elements shown in Figure 8. On the air side, the line coming from the room facilities is injected into the airbox passing through a 6kW Convectronics electric heater, in order to allow its preheat temperature as desired; and from here it gets into the injector. The fuel, on the other hand, is directly introduced into the injector after being mixed (in case that both methane and hydrogen are used) inside the manifold. This manifold has three inlets, each of them coming from each of the fuel components MFC (controlled by the microprocessor, represented

as its model number 0154), and one outlet corresponding to the fuel line going into the injector. See below for more details.

On top of the airbox, enclosing the injector, is located the quartz tube within which the combustion takes place, and where the flame is designed to be contained. On top of it, guided by four threaded rods, an upper plate encloses part of exit, leaving an open area of 1.02".

Regarding the data logging, a pressure transducer is used to monitor the pressure drop across the airbox, and two thermocouples to monitor the temperature at the bottom and top of it. Right at the exit of the quartz tube, a probe is placed so as to get the exhaust gases into the gas analyzer (Horiba PG 350) for their study.

From the imaging diagnostics point of view, the cameras are placed so as to enable the field of view across the quartz part. See next section for more details.
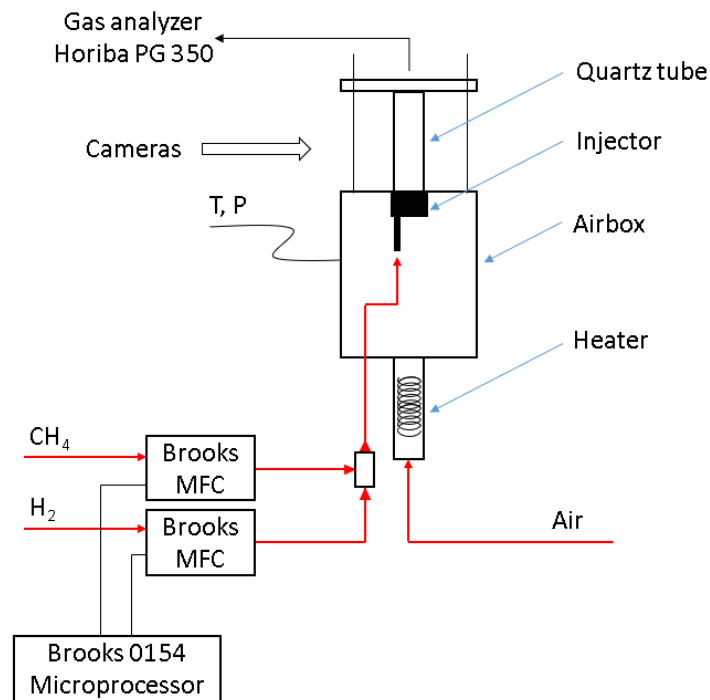
Figure 8: Test rig setup drawing.

As mentioned, both the air and fuel lines are detailed in Figure 9. Regarding the airline, it goes into the heater after the sonic orifice metering (depicted as 2 in the figure): right before the O´Keefe sonic orifice, a pressure transducer (1) is installed so as to control the upstream pressure. Equation 6 refers to the calibration curve of 1, while Equation 7 and Equation 5 are associated to 2.

On the other hand, the three fuel lines are equivalent in terms of their elements: their corresponding lines go into the mass flow controllers, followed by a check valve to avoid counter-flow from the

later manifold, in which the three lines are mixed and sent into the reducer to adapt the line size for the injector inlet. In terms of the calibration curves showed in the previous section, Equation 10, Equation 11 and Equation 12 correspond to elements 3 and 4 (both hydrogen lines are depicted as one single element in the drawing), respectively.
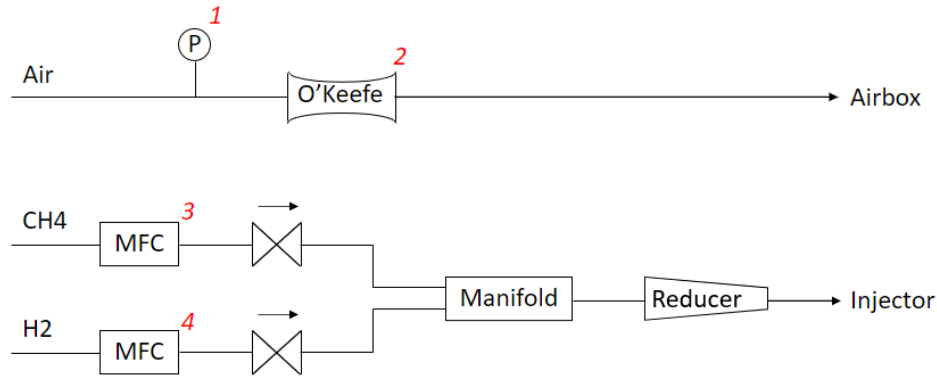
Figure 9: Air and fuel lines drawing.

4.3 Imaging diagnostics setup

After considering the many different options of cameras, Figure 10 was considered as a solution to use them all simultaneously. With the experimental rig on the middle, the needed material is intended to be sat on each of the two optical tables on the sides.

Because of the four threaded rods sketched in Figure 8, the schlieren light beam and the fields of view of the cameras must be oriented in specific directions. The drawing has been located such as the two free paths are horizontal and vertical.

First, the Z-type schlieren has the LS represented as the red dot on the top right of Figure 10, followed by the two PM as the red rectangles, the KE and the corresponding camera, all connected by the pink arrows standing for the light beams. The camera to be used for this purpose could be a conventional Nikon D-90.

In order to capture the OH* chemiluminescence, a glass is oriented at 45° with respect to the second light beam (the horizontal one, crossing the flame) in order to reflect the desired light into the OH* dedicated camera. The purpose of the glass is to allow the light to go through it, but not the OH* chemiluminescence: it occurs within the range of the UVB (280 to 315 nm), so the rays are mainly blocked by the glass. To capture this phenomena, cameras like the Dynacolor, Andor, or the Phantom with an intensifier, are considered.

For the high speed phenomena, a similar concept was considered. With the use of a different type

of glass, to allow the desired light to go through or reflect, some light beams go into the high speed camera, such as the Phantom or the Andor.

The ultimate purpose of this layout is to get all the images from the same angle of the flame, so one can easily superimpose them to get more data for each frame. Thus, the heat release captured with the OH* camera could be superimposed to the visible flame structure, and they can be linked.
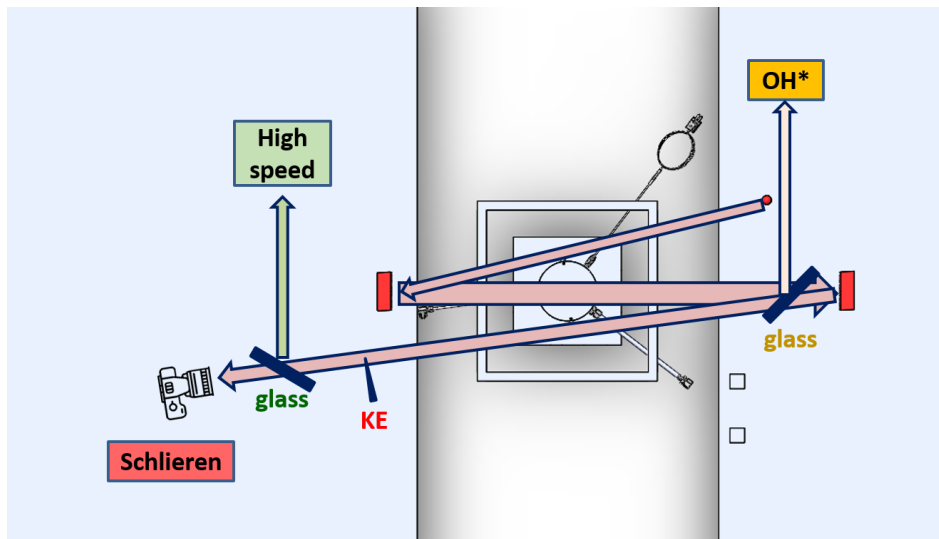
Figure 10: Initial cameras setup.

However, as it was introduced in subsection 2.4.1, the schlieren effect on round surfaces is not straight-forward, but it needs some correction lenses. Because of the complex and detailed design they require, and the first stage of the design using the round cylinder (rather than the flat windows), Figure 10 is not intended to be used at this first approach.

Figure 11 shows the final configuration of cameras that was used. On the top left part of it, one can see the three cameras that record the images simultaneously: from front to back, Phantom v7.1, Dynacolor FB-N9-U and Nikon D90. The three of them pointed towards the combustion with the same angle.
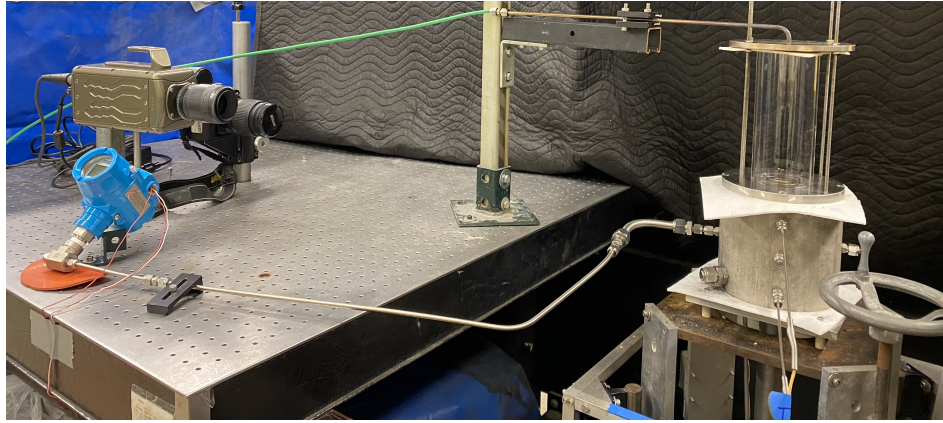
Figure 11: Cameras setup.

4.4 Experiments design

Two main sets of testing were defined at this first stage of the process: one to characterize the LBO performance of each injector, and a second one to assess their performance in terms of emissions and imaging characterization.

4.4.1 Lean blow-out limits

First, the lean blow-out limits need to be determined for each of the configurations, injector-plate, in order to determine the lower limit of the equivalence ratios. Once they are known, all the configurations can be tested so as to obtain the desired data (emissions, images...) to perform the analyses.

The lean blow off test plan was defined to be a three-level, Box-Behnken surface design, constructed using the software DesignExpert 13. A total of six factors were used: the three corresponding to the injector geometry, and three referring to the testing conditions, as shown in Table 4. The combustion conditions were defined by the airbox pressure drop, which indeed fixed the air flow rate that needed to be supplied; the preheat temperature of such air flow, which greatly contributes to determine one other parameter of interest, the adiabatic flame temperature (since the fuel is introduced into the combustion at room temperature); and the fuel composition, the percentage of hydrogen present in the mixture.

This resulted in a 15-points matrix (see Table 5), considering the three repeat points, for which the equivalence ratio at which the blow-out occurs is recorded as the response.

Table 4: Levels for the LBO factorial design.

Factor	Low	Mid	High
A - Air Split	-1	0	1
B - Fuel Swirl	-1	0	1
C - Air Swirl	-1	0	1
D - Preheat temperature [K]	465	573	675
E - Pressure drop [%]	1	4	6
F - Fuel composition [%H_2]	0	50	100

Table 5: LBO testing matrix for each injector.

Standard order	Factor 1 Pressure drop [psig]	Factor 2 Preheat T [K]	Factor 3 Fuel composition [%H_2]
1	2	465	50
2	6	465	50
3	2	675	50
4	6	675	50
5	2	573	0
6	6	573	0
7	2	573	100
8	6	573	100
9	4	465	0
10	4	675	0
11	4	465	100
12	4	675	100
13	4	573	50
14	4	573	50
15	4	573	50

4.4.2 Performance testing

On the other hand, the performance testing was also designed as a three-level, Box-Behnken design, but adding an extra factor, the adiabatic flame temperature, as shown in Table 6. This second study resulted in a 27-points matrix (see Table 7), once again with three repeated points.

Table 6: Levels for the performance factorial design.

Factor	Low	Mid	High
A - Air Split	-1	0	1
B - Fuel Swirl	-1	0	1
C - Air Swirl	-1	0	1
D - Preheat temperature [K]	465	573	675
E - Pressure drop [%]	1	4	6
F - Fuel composition [%H_2]	0	50	100
G - Adiabatic flame temperature [K]	1500	1675	1850

Table 7: Performance testing matrix for each injector.

Standard order	Factor 1 Pressure drop [psig]	Factor 2 Preheat T [K]	Factor 3 Fuel composition [%H_2]	Factor 4 Adiabatic flame T [K]
1	2	465	50	1675
2	6	465	50	1675
3	2	675	50	1675
4	6	675	50	1675
5	4	573	0	1500
6	4	573	100	1500
7	4	573	0	1850
8	4	573	100	1675
9	2	573	50	1500
10	6	573	50	1500
11	2	573	50	1850
12	6	573	50	1850
13	4	465	0	1675
14	4	675	0	1675
15	4	465	100	1500
16	4	675	100	1675
17	2	573	0	1675
18	6	573	0	1675
19	2	573	100	1675
20	6	573	100	1500
21	4	465	50	1500
22	4	675	50	1500
23	4	465	50	1850
24	4	675	50	1850
25	4	573	50	1675
26	4	573	50	1850
27	4	573	50	1850

4.5 Experimental data collection

4.5.1 Lean blow-out limits

For these tests, the only data to be collected is the LBO limit for each of the cases. Once each of the three factors are fixed, the equivalence ratio is initialized in a high enough value such that the flame is stable. Once the combustion is stabilized, ϕ is decreased gradually (by keeping the air flow constant, and decreasing the fuel flow) until the flame blows off: this is the ϕ corresponding to the LBO limit that is sought.

Regarding the pressure drop, though, the followed procedure is as follows: without any reaction initialized, the heater is set at its corresponding temperature and the air flow rate is adjusted so as to match the desired pressure drop. This airflow is the one to use for each combination of pressure drop and preheat temperature; this initial procedure is performed for each particular injector before its testing, since the required air flow will change because of the injector effective area (see Table 1).

Thus, for each injector it is required to get 9 different air flow rates, one for each combination of pressure drop (2%, 4%, 6%) and preheat temperature ($500\,K$, $650\,K$, $800\,K$).

Since the equivalence ratio is not directly controlled, but via the fuel flow rates (since the air flow rate is fixed by means of the pressure drop across the airbox), the data to be taken from each test is the fuel flow rates reading from the microprocessor. From the air and fuel flow rates, the equivalence ratio is computed.

4.5.2 Performance testing

For each of the 16 injectors, the testing matrix shown in Table 7 was followed. Each burning condition was set and stabilized before collecting the emissions and imaging data. To do so, the heater was set at the corresponding preheat temperature, and both the air and fuel lines were fixed at the conditions needed to ensure the pressure drop, fuel composition and adiabatic flame temperature.

Regarding the emissions data, the following values were recorded: CO, NO, $NO_{corrected}$ (corrected at 15% O_2), $NOx_{corrected}$ (corrected at 15% O_2), CO_2, and O_2. Except for the last two, which were expressed as a percent of the dry sample, the rest of measurements were in $ppmvd$ (parts per million by volume, dry).

On the imaging side, the three types of images that were previously introduced were recorded simultaneously. The Nikon D90 was used to capture the visible spectrum, establishing the manual mode to 2.5 shutter speed and a F4 aperture. The FB-N9-U Dynacolor camera with the Sony CMOS sensor was employed to capture the OH* chemiluminescence, using an exposure time of 999900 μs and a gain of 6 dB. The Phantom v7.1, aimed to capture the high-speed dynamics of the flame, with a sample

rate of 200 frames per second and an exposure of 4997 μs.

4.6   Experimental data analysis

4.6.1   Lean blow-out limits

First of all, regarding the LBO testing, even though the data was collected in terms of the equivalence ratio, ϕ, the data analysis was determined to be performed using the adiabatic flame temperature (AFT) at this condition. To do so, Ansys Chemkin-Pro was used: first, the equilibrium temperature of the mixture was computed using the flow rates of both the air and fuel, as well as the preheat temperature of the air. Once the equilibrium temperature was defined with the gas mixer model, it was inputted into an equilibrium model, together with the mixture equivalence ratio. The software provided the adiabatic flame temperature for each of the conditions.

Once all the conditions were processed (see Table 9), an analysis of variance (ANOVA)) was performed. ANOVA is a statistical formula to compare the variances across the means of different groups, aimed to determined if there is any significant difference between the means. The outcome of this study is the so-called F statistic, a ratio between "within group variance" and "between group variance": a large F-ratio means that there is a significant difference between groups, whereas a small ratio means that the null hypothesis is supported (no significant difference). This statistical study could be performed manually, but DesignExpert v13 was used to facilitate and speed up the process. The AFT response was studied in terms of the six factors shown in Table 4, in order to get the model that describes the response in terms of the significant factors. Each factor, or factor interaction, was considered as significant if its statistical p-value was lower than 0.05. This p-value represents the probability of obtaining an F-ratio large enough to have a significant difference between means.

4.6.2   Performance testing

On the other hand, the second set of testing requires some more analysis on the recorded images.

Because of the significance of the OH* chemiluminescence images (see subsection 2.4.2), the main focus was over the Dynacolor images. A Matlab code was developed to process the images and extract the flame characteristics of interest (detailed next in subsection 5.2.4).

Once all the imaging responses were extracted, DesignExpert was used again to get the statistical model with the factors listed in Table 6. Again, p-values lower than 0.05 made the factors or factors interactions considered as significant.

Apart from the models to get the imaging responses as functions of the testing conditions, a further step was performed linking the OH* responses and the emissions. More specifically, the NOx emissions

were modeled as a function of the testing conditions and the imaging responses.

This latter coupling between emissions and imaging was further exploited with a Matlab script to plot the emissions versus some of the imaging responses, to examine particular relationships.

Additionally, because of the complexity of the DesignExpert model, some machine learning techniques were examined to result into the sought model. The overall target would be a model that can predict the emissions based on the combustion characteristics and the imaging responses, without needing a designated gas analyzer.

Results. Data collection

5.1 LBO testing

Table 8 presents the LBO response for each of the 16 injector configurations (referred to as in each column), according to the standard order (*std* column) shown in Table 5. On the other hand, Table 9 shows the corresponding AFT (adiabatic flame temperature) for each of the points shown in Table 8, in Kelvin. Both tables graphically represent the heat map associated with their values: the greener the cell, the lower the equivalence ratio and adiabatic flame temperature, respectively. This system was employed during the testing to detect any significant outliers on each injector, since the same pattern was expected and observed throughout the testing matrix.

Table 8: LBO testing data.

Std	#1	#2	#3	#4	#5	#6	#7	#8	#9	#10	#11	#12	#13	#14	#15	#16
1	0.1481	0.1424	0.1840	0.2430	0.1308	0.2318	0.3620	0.1535	0.1685	0.3061	0.1298	0.1291	0.2645	0.3699	0.1860	0.1415
2	0.1837	0.1568	0.2141	0.2974	0.1499	0.2709	0.4218	0.1842	0.2086	0.3024	0.1507	0.1555	0.3212	0.4129	0.2282	0.1580
3	0.1170	0.1117	0.1505	0.1777	0.1055	0.1838	0.2493	0.1137	0.1428	0.1820	0.1072	0.0883	0.1957	0.2617	0.1524	0.1087
4	0.1566	0.1276	0.1735	0.2216	0.1249	0.2215	0.3098	0.1695	0.1878	0.2243	0.1258	0.1316	0.2396	0.3141	0.2012	0.1352
5	0.2096	0.1876	0.2374	0.3096	0.1800	0.3066	0.4671	0.2062	0.2264	0.3065	0.1797	0.1747	0.3466	0.4730	0.2424	0.1821
6	0.2935	0.2236	0.2933	0.3959	0.3034	0.3727	0.5173	0.2673	0.3088	0.4019	0.3095	0.2327	0.4281	0.5181	0.3188	0.2196
7	0.0113	0.0231	0.0092	0.0927	0.0166	0.0997	0.1273	0.0058	0.0106	0.0967	0.0095	0.0075	0.1063	0.1318	0.0055	0.0168
8	0.0381	0.0735	0.0938		0.0659			0.0214	0.0403		0.0656	0.0220			0.0270	0.0741
9	0.3170	0.3259	0.3262	0.4217	0.3106	0.4028	0.5433	0.3157	0.3645	0.4295	0.3290	0.2843	0.4521	0.5531	0.3440	0.3154
10	0.2322	0.1860	0.2468	0.3174	0.1767	0.3216	0.4377	0.2272	0.2686	0.3079	0.1751	0.1944	0.3557	0.4496	0.2764	0.1841
11	0.0592	0.0762	0.1055	0.1165	0.0739			0.0276	0.0582		0.0713	0.0248			0.0365	0.0783
12	0.0154	0.0206	0.0177	0.0896	0.0234	0.0966	0.1168	0.0077	0.0141	0.0906	0.0127	0.0097	0.0965	0.1190	0.0100	0.0159
13	0.1727	0.1420	0.1925	0.2371	0.1333	0.2446	0.3472	0.1748	0.1936	0.2420	0.1369	0.1399	0.2608	0.3513	0.2101	0.1409
14	0.1738	0.1418	0.1967	0.2355	0.1333	0.2476	0.3472	0.1762	0.1963	0.2404	0.1356	0.1425	0.2653	0.3556	0.2101	0.1437
15	0.1725	0.1391	0.1952	0.2355	0.1348	0.2461	0.3456	0.1748	0.1937	0.2405	0.1369	0.1397	0.2578	0.3455	0.2071	0.1409

Table 9: AFT [K] of LBO testing data.

Std	#1	#2	#3	#4	#5	#6	#7	#8	#9	#10	#11	#12	#13	#14	#15	#16
1	867.30	852.79	956.02	1095.65	823.41	1069.81	1357.96	880.83	918.07	1238.32	820.77	819.09	1144.94	1374.50	960.84	850.60
2	955.33	889.14	1028.07	1218.60	871.80	1159.37	1480.88	956.46	1015.19	1229.66	873.77	885.85	1270.81	1462.85	1061.40	891.95
3	978.83	965.58	1059.77	1123.66	950.41	1137.94	1285.62	970.61	1041.37	1133.68	954.72	907.45	1165.33	1312.80	1064.29	958.42
4	1074.20	1004.80	1114.06	1224.24	998.12	1224.01	1415.56	1104.60	1147.18	1230.27	1000.42	1014.48	1264.25	1424.50	1178.01	1023.02
5	1091.85	1041.68	1153.64	1308.69	1024.33	1302.47	1619.74	1084.09	1129.44	1302.32	1023.61	1012.11	1385.07	1630.71	1164.69	1028.26
6	1274.89	1123.15	1274.40	1483.59	1295.67	1437.58	1711.58	1218.87	1307.09	1495.30	1308.60	1143.26	1546.06	1712.97	1327.92	1114.18
7	608.99	646.82	603.50	859.00	626.21	879.29	957.77	591.20	606.91	870.51	603.16	596.74	898.21	970.28	590.48	626.94
8	694.69	802.72	862.58		780.00			640.52	701.49		778.89	642.34			659.58	800.90
9	1236.87	1255.63	1256.24	1450.86	1223.11	1413.39	1680.18	1234.07	1336.02	1466.25	1262.14	1165.61	1510.14	1697.78	1293.63	1233.31
10	1229.13	1127.44	1260.71	1408.05	1106.34	1416.71	1642.31	1218.44	1306.96	1388.75	1102.73	1146.19	1493.39	1664.35	1323.44	1123.06
11	657.72	710.32	798.79	831.24	703.35			556.44	654.50		695.21	547.20			585.19	716.79
12	722.81	738.96	730.05	943.27	747.53	963.30	1019.58	698.80	718.77	946.15	714.35	705.06	962.87	1025.65	706.00	724.27
13	1022.59	948.29	1069.61	1172.66	926.70	1189.69	1411.75	1027.71	1072.17	1183.86	935.76	943.19	1225.94	1420.40	1110.71	945.61
14	1025.36	947.64	1079.48	1169.07	926.69	1196.29	1411.74	1031.03	1078.53	1180.05	932.53	949.37	1235.94	1429.16	1110.70	952.42
15	1022.27	941.22	1076.09	1169.08	930.57	1192.99	1408.42	1027.70	1072.47	1180.35	935.75	942.56	1219.23	1408.27	1103.73	945.60

It can be observed that there are mainly four cases that showed lean responses: standard orders 7, 8,

11 and 12. As one can read from Table 5, these correspond to the hydrogen combustion points. Some of these points, though, could not be recorded (as observed by the blank cells on the table) because of the limited maximum flow rate of the mass flow controller: By the time this testing was performed, only one of the two hydrogen MFCs was available (the one with a maximum flow rate of 20 SCFM), so it was not possible to achieve the fuel-to-air ratio to sustain the flame under the given conditions.

Additionally, some outliers were detected on these hydrogen conditions: standard points 7 and 12, especially, for injectors 3, 8 and 12, among others. It can read that their ϕ_{LBO} were extremely low, in the order of 0.00x. Because of the high diffusivity of hydrogen, the LBO was registered when the very last flame spot was extinguished, even though that was clearly off from a premixed flame. This non-premixed behavior is clearly represented in Figure 12: the sequence of the hydrogen LBO approach captured with the UV sensitive camera, where the brightest regions correspond to the different flame spots situated on top of the fuel ports of the injectors. Matlab's colormap was applied to each frame to help visualize the gradient from the monochromatic images.
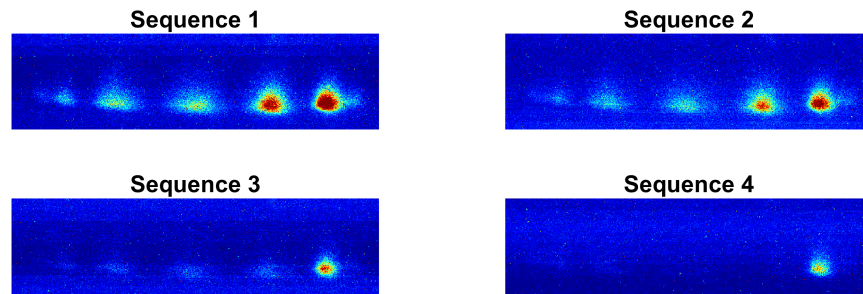
Figure 12: Sequence of OH* images before reaching the non-uniform H_2 LBO.

5.2 Injectors testing

5.2.1 Phantom camera imaging

This section exemplifies one frame of the high speed recordings captured with the Phantom v7.1 camera, for each of the three fuel compositions that were tested. Figure 13a shows standard order 5 (natural gas combustion, 4% pressure drop, 573K preheat temperature, and 1500K adiabatic flame temperature), Figure 13b shows standard order 1 (50% natural gas and 50% hydrogen, 2% pressure drop, 465K preheat temperature, and 1675K adiabatic flame temperature) and Figure 13c shows standard order 6 (hydrogen combustion, 4% pressure drop, 573K preheat temperature, and 1500K adiabatic flame temperature), all of them for injector 3, the midpoint of the hardware set.
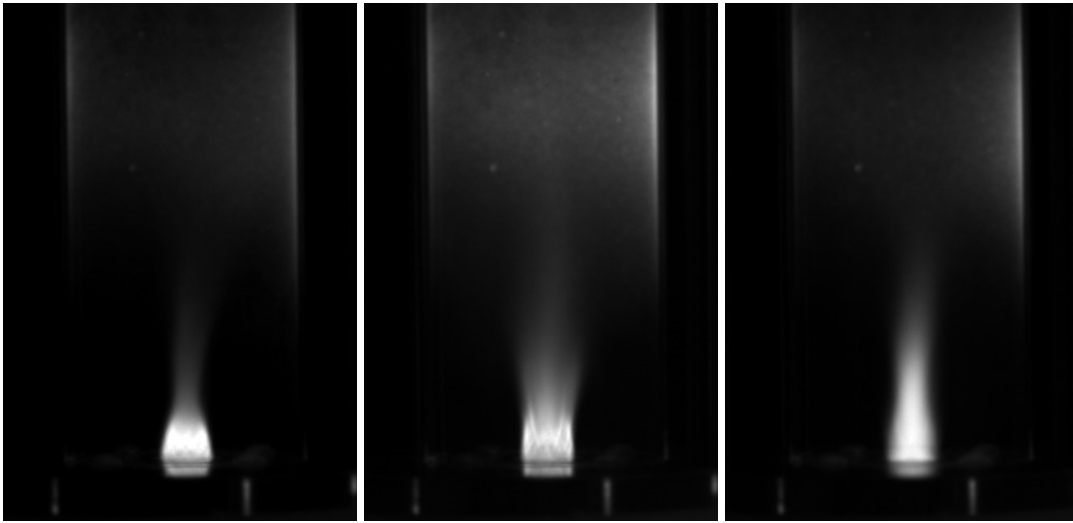
(a) Natural gas combustion, standard point 5.

(b) 50% CH4 and 50% H2 combustion, standard point 1.

(c) Hydrogen combustion, standard point 6.

Figure 13: High speed frames recorded with Phantom v7.1, from injector 3.

5.2.2   Nikon D90 camera imaging

This section exemplifies one frame of the UV spectrum captured with the Dynacolor camera, for each of the three fuel compositions that were tested. Figure 14a shows standard order 5 (natural gas combustion, 4% pressure drop, 573K preheat temperature, and 1500K adiabatic flame temperature), Figure 14b shows standard order 1 (50% natural gas and 50% hydrogen, 2% pressure drop, 465K preheat temperature, and 1675K adiabatic flame temperature) and Figure 14c shows standard order 6 (hydrogen combustion, 4% pressure drop, 573K preheat temperature, and 1500K adiabatic flame temperature), all of them for injector 3, the midpoint of the hardware set.

5.2.3   Dynacolor camera imaging

This section exemplifies one picture of the visible spectrum captured with the Nikon D90 camera, for each of the three fuel compositions that were tested. Figure 15a shows standard order 5 (natural gas combustion, 4% pressure drop, 573K preheat temperature, and 1500K adiabatic flame temperature), Figure 15b shows standard order 1 (50% natural gas and 50% hydrogen, 2% pressure drop, 465K preheat temperature, and 1675K adiabatic flame temperature) and Figure 15c shows standard order 6 (hydrogen combustion, 4% pressure drop, 573K preheat temperature, and 1500K adiabatic flame temperature), all of them for injector 3, the midpoint of the hardware set.

(a) Natural gas combustion, standard point 5.

(b) 50% CH4 and 50% H2 combustion, standard point 1.

(c) Hydrogen combustion, standard point 6.

Figure 14: UV spectrum frames captured with Dynacolor FB-N9-U, from injector 3.
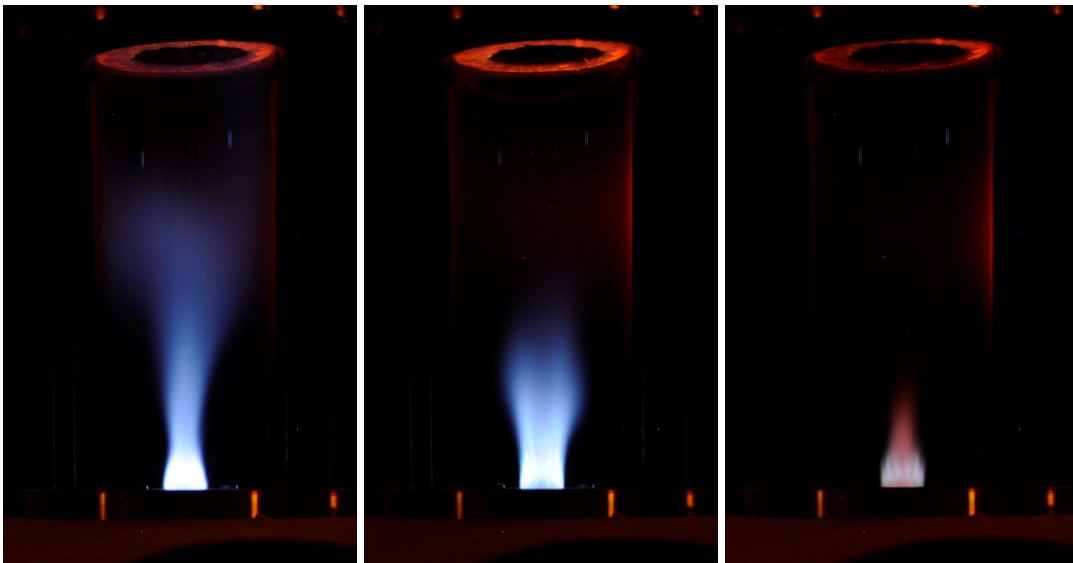
(a) Natural gas combustion, standard point 5.

(b) 50% CH4 and 50% H2 combustion, standard point 1.
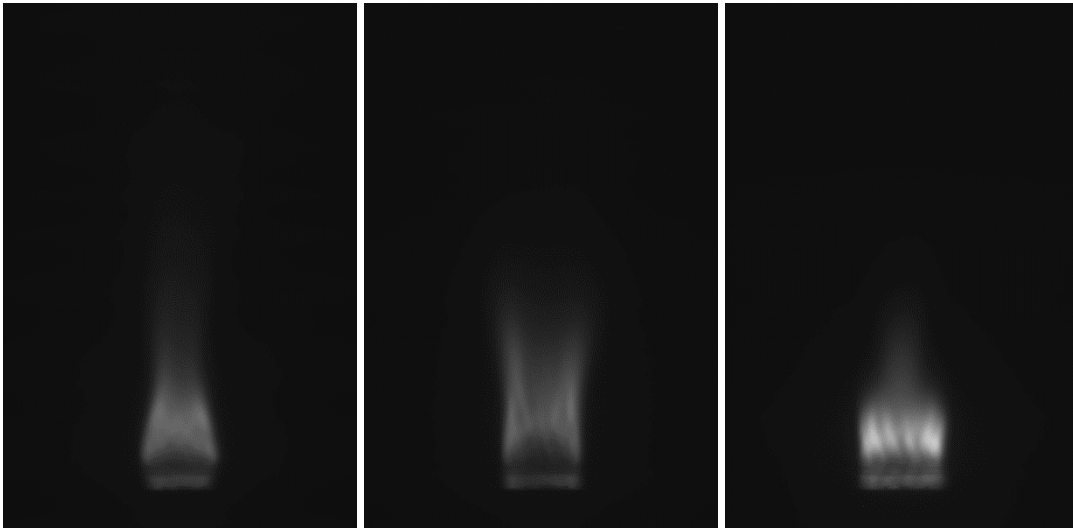
(c) Hydrogen combustion, standard point 6.

Figure 15: Visible spectrum images captured with Nikon D90, from injector 3.

5.2.4 Imaging processing

OH* chemiluminescence images were postprocessed using a Matlab script. First, Otsu's method was used to determine the brightness threshold from which a pixel should be considered as part of the flame, or just as the background: this was used to obtain a binary set of pixels (flame versus no flame), from which the flame contour was extracted (see the white contour in Figure 16c). A kernel was used so as to implement the neighbor averaging [63] and thus accommodate minor sources of random noise. This flame area was quantified by counting its number of pixels. It is worth to mention that the lateral injector limits were identified in the image (see the magenta + symbols in Figure 16c), and the corresponding reflection of the plate mounting the injector was neglected from the flame area (even though its brightness was over the defined threshold). The luminous region was determined as the ratio between this flame area and the total field of view.

From this flame area, three main spots were pinpointed: the top point defining the flame height or length (see the cyan +) with respect to the injector base, and the points furthest to the left and right (green +) defining the flame width. These last two points were also characterized in terms of their height with respect to the injector base, and their horizontal location with respect to the center of the injector.

Within the flame area, the maximum brightness was identified, as well as the average gray-level (denoted as *brightness* for shortness). As defined in subsection 2.4.5, the nonuniformity of the brightness throughout the luminous region was also computed.

Based on the maximum value for each flame, the heat release area (colored in red in Figure 16c) was measured as the amount of pixels with an intensity higher than a 90% of the maximum: this can be associated with the region where the maximum heat release occurs [8]. From this subset, two specific spots were marked: the center of gravity (COG, yellow + in Figure 16c) and the leading edge (LE, white + in Figure 16c).

The center of gravity of the heat release area was defined as its geometric center (i.e., average of horizontal and vertical components of the pixels forming the area), and was characterized by its height with respect to the injector base, and its horizontal location with respect to the center of the injector.

On the other hand, the leading edge was defined as the bottom spot of this heat release area, closer to the injector base, and was just characterized by its height.

All the distances and areas were converted from pixel units into distances, by using a known distance as a reference. The outer diameter of the quartz tube liner (known to be 85 mm wide) was measured in pixels, and the conversion was computed.
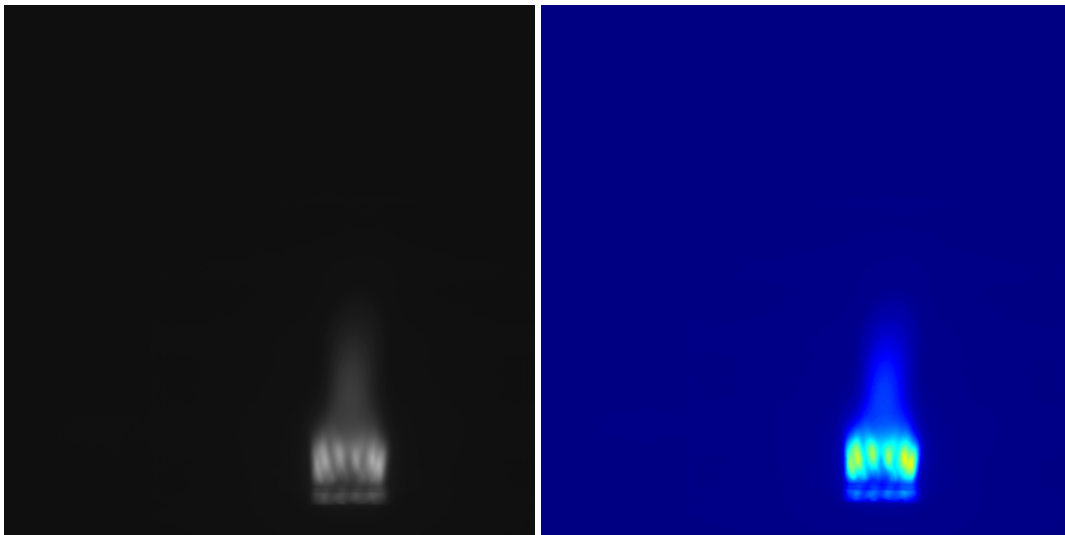
(a) Frame captured with Dynacolor camera.

(b) Matlab's colormap applied to Figure 16a.

Height = 37.21 mm
Width = 23.81 mm
  Left height = 10.01 mm
  Left width = 1.64 mm
  Right height = 9.78 mm
  Right width = 1.92 mm
Flame area = 573.39 mm^2
  Luminous region = 2.15 %
Heat release area = 10.88 mm^2
  Heat release area / flame area = 1.898 %

Maximum Brightness (0-255) = 175
Average Brightness (0-255) = 88.48
COG height = 6.55 mm
COG horizontal = 6.55 mm
LE height = 6.55 mm
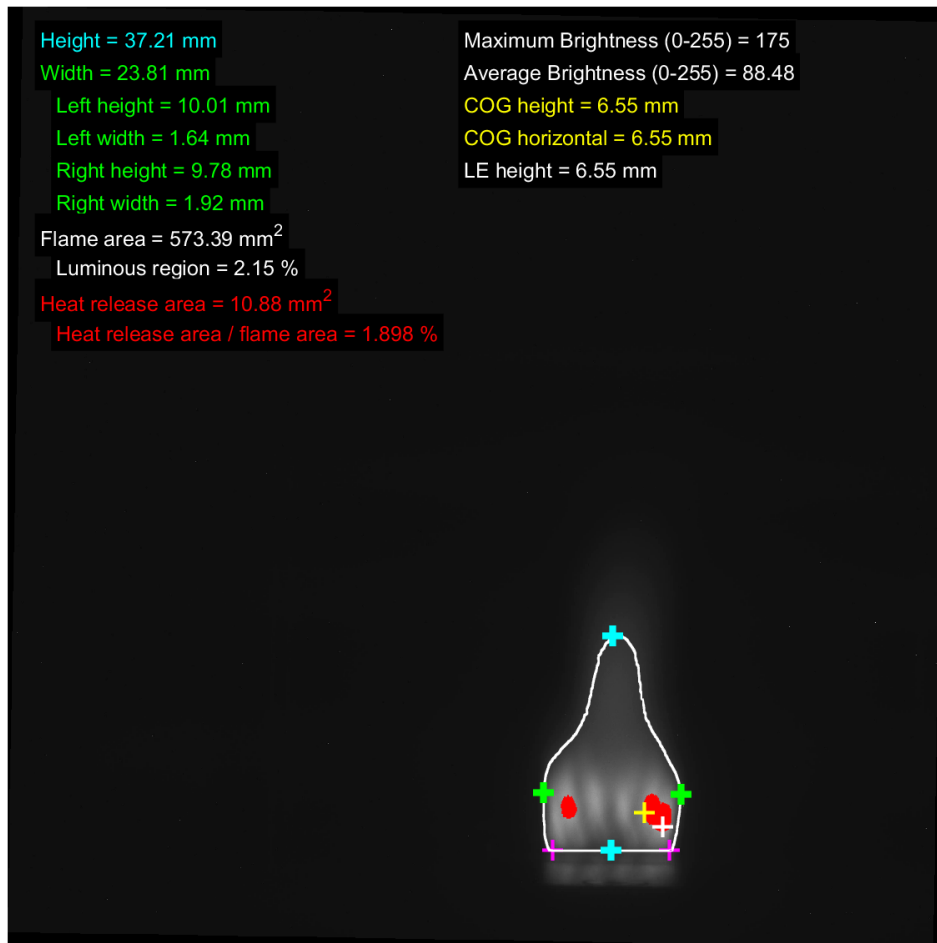
(c) Imaging responses from Figure 16a.

Figure 16: OH* chemiluminescence images from standard point 19, injector 3.

A loop was created to go through all the images for each injector, and their responses were saved into a spreadsheet for their later analysis.

As shown in Figure 16b, and was previously shown in Figure 12, Matlab's colormap function was also used to help visualizing the brightness gradients from the monochromatic images captured with Dynacolor camera. From dark blue up to red, the rainbow represents the pixel intensity from 0 to 255.

5.2.5 Emissions

As it was previously introduced, emissions data was recorded for each test point by manually recording CO, NO, $NO_{corrected}$, NOx, and $NOx_{corrected}$, as well as CO_2 and O_2 for checking purposes.

The current work is not directly focused on the emissions characterization, but NOx emissions are going to be used as a target response to be characterized.

5.3 Repeatability and uncertainties

To assess the repeatability of the data, some repeat points were recorded. Apart from those required by the testing matrix (which has 3 repeat points at the midpoint of the design space), the full LBO matrix was repeated, as well as a notorious part of the performance matrix, both for injector 3 and a total of 3 times (so 2 extra).

The average deviation of the 2 extra times with respect to the original set was considered as the repeatability of each response.

Apart from the measured repeatability, the uncertainty of the process was computed. According to [64], the uncertainty of the LBO results was found by using the partial derivatives of the independent variables on the defining equation.

For product functions,

$$R = x_1^{a_1} \cdot x_2^{a_2} \cdot \dots \cdot x_i^{a_i} \tag{18}$$

the uncertainty ω comes from

$$\omega_R = \left[\sum \left(\frac{\partial R}{\partial x_i} \omega_i \right)^2 \right]^{1/2} \tag{19}$$

By using the definition of the equivalence ratio (Equation 1), the uncertainty ω_ϕ reads as follows:

$$\frac{\omega_\phi}{\phi} = \left[\left(\frac{\omega_F \cdot 1}{F} \right)^2 + \left(\frac{\omega_A \cdot (-1)}{A} \right)^2 \right]^{1/2} = \left[\left(\frac{\omega_F}{F} \right)^2 - \left(\frac{\omega_A}{A} \right)^2 \right]^{1/2} \tag{20}$$

where A and F are the air and fuel flowrates, and ω_A and ω_F their associate uncertainties. The latter come from the precision of the pressure transducer for the air side ($\pm 0.0075\%$ of the full scale, which

was 145 psi), and the accuracy of the mass flow controllers that were used ($\pm 1\%$ of the full scale). The worst-case scenario gave an uncertainty of $\omega_{LBO} = 6.68\%$.

Regarding the emissions, the gas analyzer specified a $\pm 0.5\%$ full scale, which were: 25% O_2, 500 ppm CO, 50 ppm NO and 50 ppm NOx. This yielded into an average uncertainty of 11.1%.

Part 6

Results and discussion

6.1   Lean blow-out study

DesignExpert was used to perform the statistical study of the data from Table 8 and Table 9, as introduced before. The overall idea of the hardware design space was to draw the main conclusions with injectors 1 to 13, and then use 14 to 16 to test and verify the models. Thus, an adiabatic flame temperature prediction model was sought. These models will then be used to study how the stability of the injector affects its performance.

According to the nomenclature of Table 4, the model describing the LBO equivalence ratio, ϕ_{LBO}, was given by Equation 21. All six factors (A through F) were found to be significant, as well as the AC, AF, CE, EF interactions, B^2, C^2, D^2, and F^2.

This model gave deviations of 2.89%, 9.46%, and 12.46% for injectors 14, 15, and 16, respectively. These figures do not consider the hydrogen cases (because of their nonpremixed behavior). The maximum deviations for hydrogen points were found to be 30% for injector 14, 50% for 16, and 3.69 times higher than the measured for injector 15.

The repeatability of these results had a standard deviation of 1.45%.

$$
\begin{aligned}
\phi_{LBO} = \Big[& 0.2517 + 0.0627A - 0.0035B + 0.0487C + 0.0245D - 0.0323E - 0.1351F \\
& + 0.0381AC - 0.0171AF - 0.0102CE - 0.0077DF + 0.0102EF + 0.0085B^2 \\
& + 0.0091C^2 - 0.0139D^2 - 0.0184F^2 \Big]^{1/0.83}
\end{aligned}
\tag{21}
$$

However, as mentioned, the ANOVA of interest was the one done over the adiabatic flame temperature. A linear regression was used to get the model, using all six main factors and the following interactions: AB, AC, AF, CE, DF, EF, B^2, C^2, D^2, and F^2. The resulting model presented a coefficience of variance of 4.12%, R^2 of 0.9720, adjusted R^2 of 0.9693 and predicted R^2 of 0.9654, so good predictors overall. In order of statistical significance, according to their F-value, the highest contributors to the model would be: fuel composition (F-value: 3213.17), air splits (F-value: 994.06), air swirl (F-value: 622.90), splits and air swirl interaction (F-value: 195.69), and pressure drop (F-value: 142.45), followed by F^2, AF, EF and D^2, then the preheat temperature (F-value: 19.77), and in last term the fuel swirl (F-value: 2.56) whose p-value was higher than the chosen 0.05 but it was included because of the hierarchy of the model.

Figure 17a shows the clear effect of the fuel composition on the temperature of the adiabatic flame at LBO. The greater the amount of hydrogen in the fuel composition, the lower the temperature; therefore, the more stable the combustion. This corresponds to the wider flammability limits of the hydrogen compared to those of the natural gas, its higher diffusivity (causing the nonpremixed behavior) and the higher flame speed. Low air splits (i.e., more air bypassing the injector), air swirl (i.e., more vertical air flow) and pressure drop (i.e., lower air flow velocity) also increase the stability (i.e., decrease the AFT), while the fuel swirl barely affects it.

Another important plot to mention is Figure 17b, the interaction between the air split and the air swirl. It can be observed that the effect of the air swirl is enhanced for higher levels of splits: when most of the air goes through the air ports (i.e., high air split), the air swirl has a higher effect, as the majority of the flow suffers from this geometry. If most of the air bypasses the air ports (i.e., low splits), then the geometry of these has a reduced effect.

According to this plot, thus, lower air split are preferable to increase the stability of the flame (reduce the AFT at LBO). Because of the reduced effect of the air swirl, either high or low levels would work, but if any preference was to be taken, it would be lower air swirl.

These results make sense in terms of mixing: the greater the volume of swirled air (high air splits and swirl), the greater the mixing with the fuel flowrate, and thus further from the non-premixed behavior that increases the stability of diffusive flames.

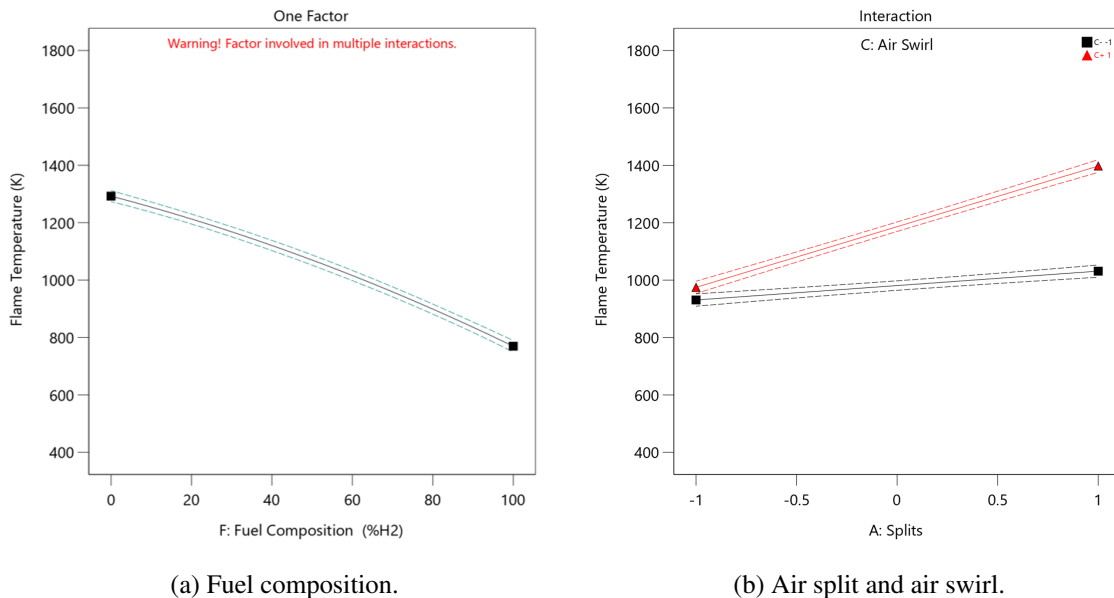(a) Fuel composition. (b) Air split and air swirl.

Figure 17: AFT at LBO - ANOVA factors.

The obtained model was then tested with injectors 14 to 16 to validate the conclusions. Unlike the

observed behavior with the hydrogen cases on the ϕ_{LBO} model, the AFT is also predicted for them with an acceptable margin of error. The average deviation for each of the three injectors was 2.18%, 4.78% and 5.87%, respectively, presenting maximums of 6.35%, 8.68%, and 14.86%.

6.1.1 Effect of confinement ratio

The previous results were all taken with a quartz liner tube of 80mm ID (inner diameter). The effect that this confinement ratio might have on the results was tested by comparing these results versus the behavior measured with a combustor of 47mm ID. Table 10 shows the results of the study.

Most of the cases showed deviations lower than the LBO uncertainty value (found to be $\omega_{LBO} = 6.68\%$), so the effect of the confinement ratio was considered negligible. The two cases showing large deviations, standards 7 and 12, correspond to the two most extreme hydrogen cases, where the non-premixed behavior was clearly identified. Thus, the latter were considered as outliers on this study.

Table 10: Confinement ratio effect on the LBO study.

Standard order	80mm ID ϕ_{LBO}	47mm ID ϕ_{LBO}	Deviation [%]
1	0.1864	0.1840	1.29
2	0.2173	0.2141	1.53
3	0.1549	0.1505	2.91
4	0.1762	0.1735	1.51
5	0.2507	0.2374	5.64
6	0.3135	0.2933	6.89
7	0.0822	0.0092	792.94
8	0.0975	0.0938	3.88
9	0.3419	0.3262	4.83
10	0.2559	0.2468	3.68
11	0.1080	0.1055	2.40
12	0.0813	0.0177	358.33
13	0.1997	0.1925	3.76
14	0.2013	0.1967	2.34
15	0.1997	0.1952	2.29

6.2 Performance assessment

6.2.1 Imaging analysis

From the responses introduced previously, five were selected as potential significant characteristics to describe the structure of the flame: the average brightness, the flame area, the heat release area, and the leading edge and the center of gravity of the heat release area. An analysis of variance (ANOVA) was performed for each of them, using as factors the combustion conditions and the features of the injector geometry. To do so, just injectors 1 to 13 were used, in order to keep the last 3 injectors as validation for the obtained models. The simplified, coded equations are shown below, using factors A through F of Table 4 ranging from -1 to 1 according to their corresponding levels.

$$Average\ brightness = 173.48 + 26.24D + 42.01E + 45.61F + 0.24G \tag{22}$$
$$+ 13.45DE - 4.48EG - 7.61D^2 + 13.16F^2$$

$$Flame\ area = 547 + 41.22D - 156.40E - 111.24F + 98.08G - 63.53DF - 110.18EG - 95.81FG \tag{23}$$

$$Heat\ release\ area = 17.17 + 5.30D + 1.06E + 12.33G + 6.26DG + 7.75EG + 7.49G^2 \tag{24}$$

$$Leading\ edge = \frac{1}{0.1938 + 0.0466E + 0.0609F - 0.0258G} \tag{25}$$

$$Center\ of\ gravity = e^{2.18 - 0.0008D - 0.2371E - 0.3315F + 0.1941F + 0.0737D^2 + 0.0847G^2} \tag{26}$$

Each of these responses presented a variability of 9.97% for brightness, 8.91% and 31.59% for the COG and LE of the heat release area, respectively, 8.59% for the flame area and 100.25% for the heat release area. These were calculated by averaging the deviation of the measured responses in three sets of tests and were used to assess the computed models. The corresponding coefficients of variance for all five responses were 7.27%, 3.15%, 19.98%, 9.79% and 24.13%, respectively, for the brightness, COG, LE, flame area, and heat release area. Therefore, by comparing variability and coefficients of variance, it can be concluded that the ANOVA models closely represented the responses as a function of the factors studied.

The brightness of the flame was identified to be mainly linearly dependent on the fuel composition F (i.e., higher contents of hydrogen) and the preheat temperature E, as shown in subsection 22,

both increasing trends. The former was linked to the higher flame speed and diffusivity of hydrogen compared to methane [65], which results in lower ignition times and therefore less time to mix and higher hot spots. The effect of the preheat temperature was again linked to a decrease in the ignition time with higher temperatures, resulting in less mixing time and a higher concentration of hot spots [66]. The dependence of brightness on pressure drop was concave down, as shown with the second-order component of D, and coupled with F in an interaction factor, as shown in Figure 18a. The higher the pressure drop, the brighter the flame because of the increased air axial velocity and the corresponding reduction in the mixing with the fuel. This increase with the pressure drop was even more pronounced for higher hydrogen content in the fuel mixture. The plot shown in Figure 18b was used to corroborate that the brighter the flame, the higher the NOx emissions, which makes sense with the mixing argument used [67]; note the increasing linear trend that agrees with the results of Liu et al. [43] (the slope and intersection of the regression vary with the combustion conditions).

(a) Fuel composition.

(b) Air split and air swirl.
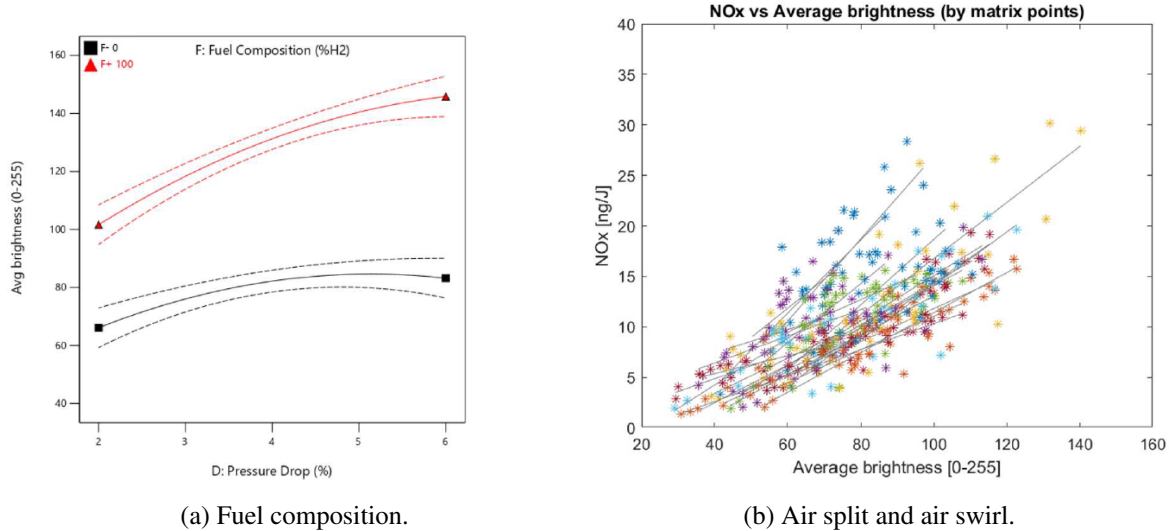
Figure 18: Average brightness study.

Regarding the flame area, the main contributor to the model was the preheat temperature (with a decreasing linear component), followed by the fuel composition (again, linearly decreasing with the hydrogen content) and the flame temperature (increasing trend in this case). The former is in agreement with the previous argument, since a more compact area was obtained due to the reduced ignition time. Hydrogen flames were more compact than natural gas or blends, again in agreement with the higher reactivity argument. This effect of the fuel composition was decreased at lower adiabatic flame temperatures, since the natural gas flames were also compact at these lower AFT levels. The interaction of the preheat and adiabatic flame temperatures was also significant: At low AFTs, the effect of the preheat was reduced, whereas higher AFTs enhanced the effect of the preheat. The adiabatic flame temperature was expected (and observed) to generally increase the flame area because of the linkage

between the OH* chemiluminescence (images that are being analyzed) and the rate of heat release: The higher the AFT, the higher the heat release of the flame, and therefore the more intense the OH* chemiluminescence recordings.

The heat release area followed a pattern quite similar to that of the flame area, with some differences. In case of the pressure drop, in this case it always increased the area, whereas for the flame area it depended on the fuel composition (it increased the area for natural gas flames but slightly decreased it for hydrogen flames). At higher flame temperatures, the heat release area increased with the preheat, but it decreased at lower levels: this was inconsistent with the previous explanation for the flame area and the discrepancy was linked to the poor repeatability of this response. Due to this latter conclusion, the study of the heat release area was not considered a crucial response.

It is worth mentioning that, in this case, one cannot find any effect of the fuel composition. It is now known that the fuel composition drastically affected the flame brightness, but since this response was obtained using the maximum brightness for each particular case, the effect of the fuel was suppressed.

In terms of the center of gravity and the leading edge of the heat release area, the same main three factors (in the same order of relevance) that were determined in the brightness study apply. The hydrogen content made both COG and LE closer to the injector, because of the higher diffusivity of this fuel and the decreased ignition time. The adiabatic flame temperature caused these heights to increase, as observed with the increased flame area. An increase in the preheat temperature reduced the heights, because of the lower ignition times: more compact, but brighter flames occurred.

6.2.2 Imaging and emissions coupling

One of the main goals of the overall project is to assess the impact of hydrogen introduction on NOx emissions. For this reason, the current work tried to establish a relationship between the injector geometry, the combustion conditions, and the imaging responses, toward the prediction of such result. To do so, two main methodologies were applied. First, DesignExpert software was applied to determine the model representing NOx as a function of 20 factors:

- Injector geometry: (A) Air split, (B) Fuel swirl, (C) Air swirl.

- Combustion conditions: (D) Pressure drop, (E) Preheat temperature, (F) Fuel composition, (G) Flame temperature.

- Imaging responses: (H) Height, (J) Width, (K) Left height, (L) Left width, (M) Right height, (N) Right width, (O) Average brightness, (P) Maximum brightness, (Q) Flame area, (R) Heat release area, (S) Center of gravity of the heat release area, (T) Horizontal location of center of gravity, (U) Leading edge of the heat release area.

Because of the expected complexity of the model, a machine learning "black box" was sought to predict the emissions as a function of these given features or factors. Due to the reduced number of samples (688 in total), several algorithms were tested to refine the level of accuracy, using Python.

6.2.2.1 DesignExpert model

A model with a total of 166 factors and interactions was constructed, based on a cubic process order, selecting the terms with p-values lower than 0.05. Several data points were considered as outliers according to the ANOVA diagnostics, and by doing so the fit statistics looked like:

- Standard deviation: 0.1538

- Coefficient of variance: 4.77 %

- R^2: 0.9757

- Adjusted R^2: 0.9630

- Predicted R^2: 0.8530

- Adequate precision: 48.7538

The predicted and adjusted R^2 were in a reasonable agreement (within 0.2 difference) according to DesignExpert statements. The adequate precision also indicated an adequate signal-to-noise ratio.

However, the resulting model was then tested with all data points to assess its level of accuracy, and the results were not as promising as the statistics shown above. An average error of $\pm$ 4.42 ng/J was obtained, which represented a deviation of 37. 15% (i.e. an average accuracy of 62.85%).

This result was attributed to different sources of error: first, it was established that the emissions had an average uncertainty of 11.1%, then the imaging responses also presented coefficients of variance ranging up to 25%, some of the imaging responses had notorious variability ranges, etc. Apart from the responses by themselves, one has to add the statistical error coming from the model construction.

For this moderate-to-low level of accuracy and also because of the complexity of the model, some alternatives were sought by means of machine learning algorithms. These would allow performing simpler predictions, potentially: the 166 terms from the statistical model made it hard to deal with, and the chances of introducing external errors by manipulating such complex equation were also considered.

6.2.2.2 Machine Learning. Random Forest

First, a Deep Artificial Neural network was implemented. The accuracy of the model was around 50%, a quite low result because of how the deep AAN are intended to work: they work fine when a big set

of data (more than 50k records) is available for the learning process. For smaller data sets, supervised machine learning models work better.

A second algorithm was tested, a random forest model. In this case, the level of accuracy was found to be between 65 and 75%. Then, an AdaBoost regression was implemented, to end up finding levels of accuracy around 70%. Finally, a Support Vector Machine (SVM) regression was tested, showing an accuracy around 50%. Refer to subsection 2.4.6 for more details on these algorithms.

None of these methods has yet been refined, but just preliminary testing was performed to select one of them for its furthest development. Due to its higher initial performance, the Random Forest algorithm was chosen for this study case.

It is worth mentioning that up to this point, the machine learning algorithms just included the combustion conditions and the imaging responses introduced earlier. Even with this reduced set of factors, some of them actually performed better than the DesignExpert model. The following optimization of the Random Forest algorithm included the injector geometric parameters as factors, as did the previous statistical model.

After some iterations looking for a more accurate model, the following Random Forest algorithm was employed using Python's library Pandas: the label or target variable was the NOx emissions, in ng/J, and the features were those described at the beginning of the section (the 3 injector parameters, 4 combustion conditions, and 13 imaging responses). A k-fold cross-validation method was used, with $k = 10$, to optimize data usage by having such a reduced data set in terms of machine learning algorithms. Therefore, all 16 injectors could be used for model construction and testing.

An iterative process was performed to select the most suitable number of estimators (or number of decision trees), by testing 1, 10, 100 and 500, to end up finding that one hundred was performing the best, closely followed by five hundreds. The accuracy achieved was around 78%. This was considerably better than the statistical model found using DesignExpert software and quite accurate for the limits imposed by the data variability.

According to the typical Random Forest Regressor parameters,

- R^2 Training Score: 0.96

- OOB Score: 0.75

- R^2 Validation Score: 0.61

the model shows some overfitting, since the OOB and the validation set perform much worse than the training set. The R^2 scores indicate how well the model fits the data, whereas the OOB (out-of-bag) error is a measurement of the properly predicted samples in the validation set.

With the model defined, the features importances were computed, in order to see how each of the factors or features impact on the final prediction. Using the proper Python's libraries, the following plot was obtained (see Figure 19): each bar represents how much the feature contributes to the response, being the sum of all 21 bars equal to 1. One can rapidly observe the huge importance of the brightness on the NOx predictions, as it was highlighted in Figure 18b: both the maximum and average responses are highly related with the NOx emissions (contributing 21.36% and 15.46%, respectively, to the prediction), but for normalization purposes the average was selected for the previous, more detailed study, rather than just the maximum value (which could just occur on an insignificant portion of the flame). Both the center of gravity and the leading edge of the heat release area also had a significant importance on the prediction (9.92 and 8.87% importances, respectively), so their previous detailed study is therefore justified. From the testing conditions, one can see how the pressure drop (PD) predominated over the rest, with a contribution of 8.32% to the final prediction. Finally, the air split was the most relevant feature from the injector's geometry, with a 4.09% contribution.
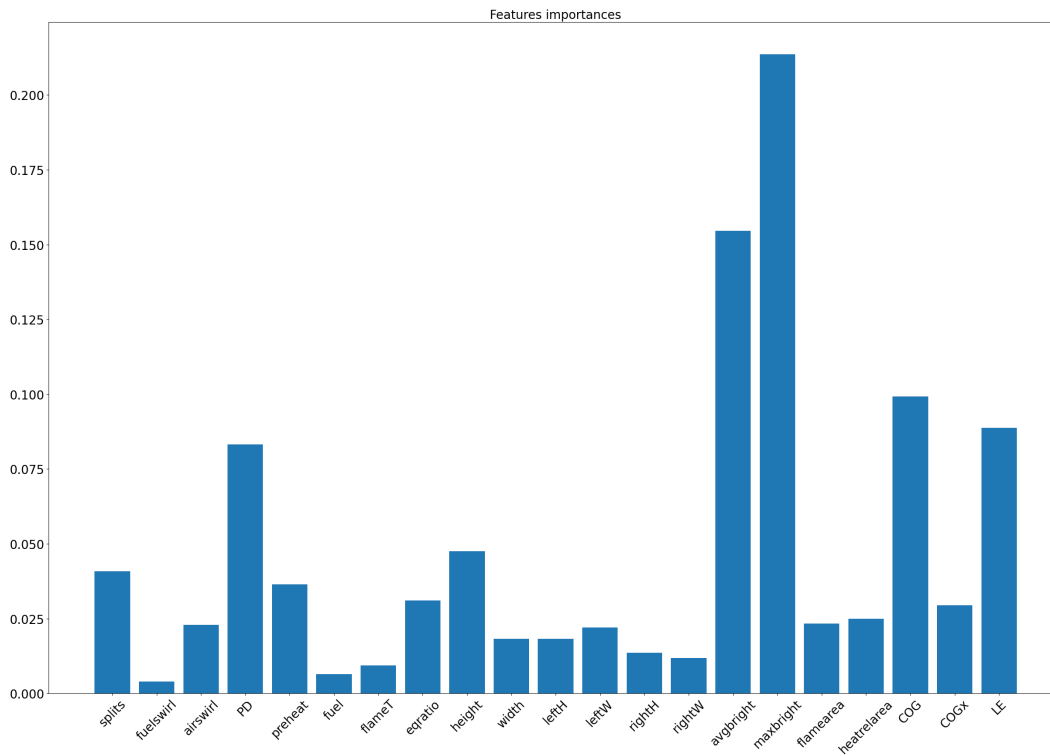
Figure 19: Features importances of the Random Forest algorithm.

For a given sample, apart from the features importances, one could also get how each of the features contribute to the prediction value. Figure 20 shown an example for a data point prediction, of an injector with air split, fuel swirl and air swirl mid-levels, and a prediction yielding to 8.69 ng/J of NOx emissions. This plot also shown the greater importance of the pressure drop and the brightness

of the flame, representing if the feature makes the predicted value to increase or decrease.

A machine learning algorithm is typically referred as a "black box" with a series of inputs and a given output, without being the end-user fully aware of how it is working towards the obtained prediction. This plot, at least, gives a sense of how each of the features contribute to such output. It has a *base* component, which would act like an offset, and then each feature contributes adding or subtracting a certain amount to it: by adding each contribution to the base, one finally gets the prediction.
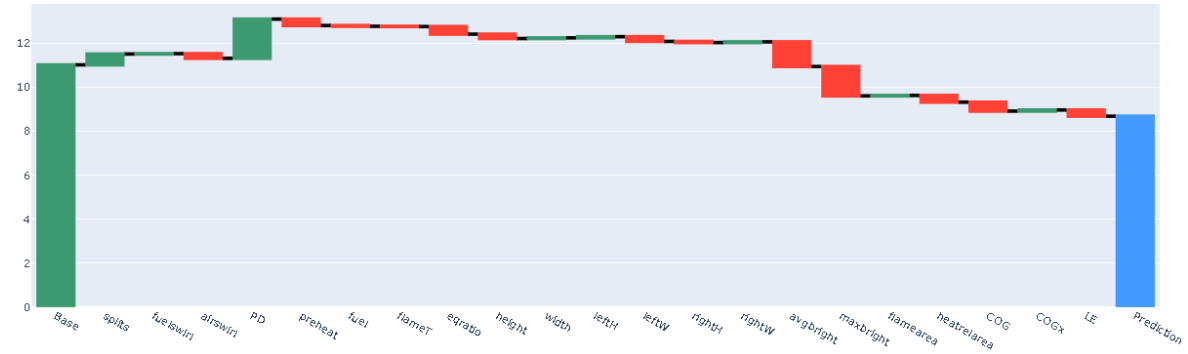

Figure 20: Features contributions for a sample.

Taking advantage of this features contributions set of information, an optimization process was sought to find the best-performing injector geometry. The overall idea was to compute the average contribution of each level (low, mid and high) for each injector factor (air split, fuel swirl, air swirl) towards the NOx formation, and thus select the level with lower emissions. Table 11 shows the average contribution of each of the factors of the injector, towards the NOx emissions predictions. It can be observed that, in order to get the lower emissions, high levels of air split and air swirl are preferred, whereas low levels of fuel swirl are desired. This same conclusion was extracted from the emissions optimization study performed in [67], which reinforces the accuracy of the used algorithm.

Table 11: Average contributions to the NOx emissions by each injector's factor.

Injector factor	Low level	Mid-level	High level
Air split	16.36	-9.63	-13.95
Fuel swirl	-0.79	0.03	0.76
Air swirl	0.98	4.34	-6.25

6.2.3 Imaging, emissions and LBO coupling

Seeking an improvement on the machine learning algorithm, the results from the stability study were included into the model. Equivalently to Equation 21, Equation 27 shows the coded equation for the

adiabatic flame temperature at the lean blow-off as a function of the splits (A), fuel swirl (B), air swirl (C), pressure drop (D), preheat temperature (E) and fuel composition (F).

$$\begin{aligned}
AFT_{LBO} = {} & 1069.95 + 130.81A - 6.59B + 102.56C + 52.98D + 19.59E \\
& - 261.51F - 13.82AB + 90.56AC - 30.87AF - 21.35CE \\
& - 17.38DF + 29.38EF + 17.14B^2 + 13.68C^2 - 29.41D^2 - 38.71F^2
\end{aligned}$$

(27)

This equation was then used to compute the AFT_{LBO} for each of the test points from the performance testing. Therefore, an extra factor or feature could be included into the predictive model.

The same Random Forest algorithm was used, being this extra feature the only difference with the previously described algorithm. No improvement was observed in terms of the obtained accuracy, again being around an 78%. This conclusion is reasonable, since the LBO model actually depends on some of the features that the machine learning algorithm already incorporated, so it is not introducing any extra information that can be used to predict the emissions. Therefore, coupling the LBO data into the imaging and emissions model is not increasing the performance of the prediction.

Part 7

Summary, Conclusions and Next steps

7.1   Summary

The sixteen injectors were able to operate on natural gas, hydrogen, and any fuel blend in between, showing a solid design concept and appropriate adaptation from the previous model. Hydrogen had a lower lean blow-out limit, as originally expected because of its wider flammability limit. A clear difference was observed in the spectrum of lean hydrogen combustion flames with respect to natural gas, which enhanced the need for imaging studies of such reactions.

Because of the weak visible spectrum of hydrogen combustion flames, OH* chemiluminescence was selected as the reference imaging technique for this study. Furthermore, since this emission is linked to exothermic reactions, it is a good index of the rate of heat release, and so it can be used as a flame front indicator. The imaging parameters can be kept constant, so direct comparison is facilitated between the wide variability of the flames. The flame brightness of the UV-spectrum images was directly correlated with the NOx emissions, so it was a convenient representative response image for the later coupling between the imaging and emissions. Other responses such as the size of the flame and the spatial location of the heat release area were also determined as significant.

As reflected in the correlation between the flame brightness and NOx emissions, the maximum and average brightness of the flame were the two responses with a higher impact on the prediction: the linear increasing trend of NOx as a function of OH* brightness from the literature was confirmed in this study. They were followed by the location of the heat release area, thus supporting the argument that has been used linking this vertical location with the level of mix of air and fuel: the closer the flame to the injector, the lower the mixing time, and therefore the greater the emissions. In terms of the combustion conditions and injector geometry, the pressure drop and air split were predominant, respectively, because of the detrimental effect of the air axial velocity on the mixing (and therefore the NOx emissions) and the improvement of the mixing with the inner air.

A machine learning random forest algorithm was constructed using the injector geometry, combustion conditions, and imaging responses as input features. This model predicted NOx emissions as output, with an overall accuracy of about 78%. The introduction of the injector's LBO limits did not add any significant improvement to the model, since this was a dependent variable on the rest of inputs.

7.2   Conclusions

The goals or research questions established in the Introduction are listed and answered here.

1. *Assessment of the lean blow-out limits of the different injectors, operating under a range of combustion conditions, and their effect on the injector performance.*

   (a) *Can the supplied injectors operate on 100% hydrogen fuels?*

   All 16 injectors were tested in 100% hydrogen conditions, and all showed their capabilities in such fuel operation. Therefore, it can be concluded that Collins Aerospace did an outstanding job of deriving the gas injectors from the original liquid injection concept. This fact allowed the incorporation of the whole set of hardware into the performance testing.

   Not as a determinant factor, but the OH* imaging allowed to assess some critical behavior from the hydrogen reactions when reaching the LBO limit.

   (b) *How is the injector geometry affecting the stability of the combustion?*

   The stability of the combustion was analyzed in terms of the adiabatic flame temperature at which the LBO occurred.

   Both air split and air swirl had a relevant impact on the LBO performance of the injector, and so did their interaction. Higher levels of either factor increased the flame temperature at the LBO, which implies a reduction of the lower stability limit: Low levels of air split and air swirl were preferred to enhance the LBO stability. However, their interaction stated that the effect of the air swirl was highly dependent on the air split: for low air splits (i.e., less air flowing through the interior passages), the significance of the air swirl (i.e., the inclination angle of the air passages) was minimum, which makes sense as less air is affected by it. However, for high air splits, the detrimental effect of increasing the air swirl had a major impact.

   However, even though the statistical p-value of the fuel swirl stated that it was not a significant factor for the model, it had to be included in the model to ensure the hierarchy. Therefore, its effect on the LBO stability could be considered as negligible.

   (c) *How are the operating conditions affecting the stability of the combustion?*

   The fuel composition was the most significant factor of the six studied (three times more than the second, according to its statistical F-value). The higher the hydrogen content on the fuel, the lower the flame temperature at LBO, so the more stable the lean combustion. However, this fact was also associated to the nonpremixed behavior that some hydrogen

57

data points experienced, which allowed the diffusive flames to last longer compared to the natural gas scenarios. This was linked to the higher reactivity of the hydrogen, as well as its wider flammability limits and higher flame speed.

The pressure drop also had a significant effect on LBO: Low levels (i.e., lower air flow velocities) were preferred to increase stability. On the other hand, the preheat temperature had a reduced effect on this response, its F-value being two orders of magnitude lower than the fuel composition.

(d) *Can a model be extracted to explain, or predict the stability behavior based on the testing factors?*

Yes, a model was derived from the statistical analysis of variance using the first 13 injectors, and then it was evaluated with the additional 3. The adiabatic flame temperature at the LBO limit could be predicted for all the studied cases within an acceptable margin of error, even for hydrogen cases showing a non-premixed behavior. The average deviation for each of the three tested injectors was 2.18%, 4.78% and 5.87%, respectively, showing maximum deviations of 6.35%, 8.68% and 14.86%.

2. *Characterization of the reaction flames by means of different imaging techniques.*

(a) *Find an imaging technique that can be used to record the wide variability of flames that result from the testing design.*

Because of the reduced visibility of the hydrogen flames, the OH* chemiluminescence was used to describe all the testing conditions. Camera parameters were fixed throughout the testing matrix to facilitate direct comparison between cases, selecting values that allowed visualization of all cases.

A different technique was also tested, the z-type schlieren. However, due to (1) the limited visibility window caused by the post holding the flat windows, (2) the elevated heating of the metallic posts, (3) the noise created by the quartz windows, and (4) the high sensitivity of the schlieren imaging to the heat release, it was not used for the quantitative analysis of the flames.

(b) *Determine the representative imaging responses to characterize the flames.*

From the different imaging responses that were extracted from each frame, its was concluded that the average brightness was a good flame characterization. This was mainly associated to the direct link between the OH* chemiluminescence intensity and the rate of heat release, so capturing the average luminosity of the flame could give a preliminary understanding of the level of heat release of the flame.

The overall flame area was also selected as a representative response. Although the defined heat release area was not considered significant due to its wide variability (reduced repeatability), its characterization by means of the center of gravity (i.e., the geometric center) and leading edge (i.e., the closest point to the injector) was remarkable.

(c) *What are the factors that affect the selected imaging responses and how do they change them?*

The average brightness was mainly affected by the fuel composition and the preheat temperature. Both factors presented increasing linear trends: The higher the hydrogen content and the preheat temperatures, the brighter the flame. The former can be linked to the higher flame speed and diffusivity of this fuel, resulting in lower ignition times and the corresponding decrease in mixing time. The latter comes with the decrease in ignition time with higher temperatures, as stated in the literature. Higher pressure drops also increased the average brightness of the flame because of the decreased mixing time because the air had a greater axial speed: the increase was quadratic and specially pronounced for higher contents of hydrogen. The adiabatic flame temperature had a minor effect on this response.

The flame area was mainly characterized by the preheat temperature (decreasing linear component), the fuel composition (decreasing linear component), and the adiabatic flame temperature (increasing linear component). The interactions between the preheat temperature and the adiabatic flame temperature, and between the fuel composition and the adiabatic flame temperature, were also remarkable for the model construction. The pressure drop was also significant to the response, although with a less intense component.

The leading edge was dependent on the preheat temperature, the fuel composition, and the adiabatic flame temperature. The pressure drop was not significant for this response.

Finally, the center of gravity was again dependent on the preheat temperature, the fuel composition, and the adiabatic flame temperature. The pressure drop had a slight significance with a quadratic term but was an order of magnitude lower than the previous three factors.

3. *Is it possible to predict the NOx emissions based on the injector factors and their LBO stability, the operating conditions and the imaging study of the flames?*

The recorded NOx emissions were compared to two different approaches for their prediction. First, an ANOVA model with injector factors, operating conditions, and all OH* chemiluminescence imaging responses was constructed. Then, with a machine learning, random forest algorithm.

The ANOVA resulted in an accuracy of 62.85%, with an average deviation of ± 4.42 ng/J. This was achieved with a complex model, composed of 166 terms up to cubic terms with p-values lower than 0.05.

On the other hand, the random forest algorithm was improved to a precision of almost 80%. This was a promising result considering the variability of both the recorded emissions (established to be around an 11%) and the imaging responses used.

This model concluded that the optimal injector factors to decrease NOx emissions were high levels of air split and air swirl, and low levels of fuel swirl (even though the latter was not as important as the first two). This conclusion was also extracted from the emissions study itself.

Regarding the LBO stability of the injectors, since it was characterized by using the same factors that were later used as features for the predictive models, no extra value was added.

(a) *What are the most relevant imaging responses to this correlation?*

The most significant responses to the machine learning correlation were both the maximum and average brightness of the flame. This was in agreement with the correlation between NOx emissions and OH* chemiluminescence, established in the literature and corroborated in the current study. The center of gravity of the heat release area was also relevant for the prediction of the NOx emissions as well as its leading edge. Regarding the injector geometry, air split was predominant, followed by air swirl. The fuel swirl had a minor effect. Finally, in terms of combustion conditions, the pressure drop was predominant, followed by the preheat and adiabatic flame temperatures.

7.3 Recommendations

As future steps for the imaging characterization of the reaction flames, it could be considered to further develop the schlieren technique for round cylinders. There are some studies in the literature that implemented some corrections to avoid the interference created by the rounded surface, but because of their complexity and the available alternatives, they were not further considered.

Alternatively, other cameras or imaging techniques could be used, such as a CMOS camera with an intensifier. This could be focused on the comparison with the novel Dynacolor model that was tested. It would be great to show this comparison between these two models and see if the quality improvement is worth the price difference (being the Dynacolor camera that was used 10 times cheaper than the other reference).

Collins Aerospace was given the guidelines found at UCI, and is going to design and manufacture two other injectors varying the levels of the used factors on the desired trend lines, to see if they

perform as expected (even better than those tested). Therefore, the constructed models will be tested by predicting the emissions with the new set of data. To do so, OH* chemiluminescence images are going to be taken for each configuration and test with the same parameters that were used in the current effort.

Finally, in order to establish a baseline for hydrogen emissions similar to the Leonard and Stegmaier's for natural gas, a premixer is set to be designed and tested for conditions similar to those exposed here. Some of the arguments for the higher emissions of hydrogen compared to natural gas were based on the level of mixedness; therefore, to support them, the combustion conditions are intended to be replicated but adding a premixing region before combustion. To support the mixedness argument that has been used during this study and the corresponding published papers, OH* chemiluminescence imaging is going to be processed to determine if the premixed flames are less bright than those that are not premixed and if their heat release area is closer to the injector.

Bibliography

1. ABUDU, Kamal et al. Impact of gas turbine flexibility improvements on combined cycle gas turbine performance. *Applied Thermal Engineering*. 2021, vol. 189, no. February, p. 116703. ISSN 13594311. Available from DOI: `10.1016/j.applthermaleng.2021.116703`.

2. XING, Chang et al. Effect of fuel flexibility on combustion performance of a micro-mixing gas turbine combustor at different fuel temperatures. *Journal of the Energy Institute*. 2022, vol. 102, no. February, pp. 100–117. ISSN 17460220. Available from DOI: `10.1016/j.joei.2022.02.010`.

3. CHOI, Jaehong et al. Flame structure and NOx emission characteristics in a single hydrogen combustor. *International Journal of Hydrogen Energy*. 2022. ISSN 0360-3199. Available from DOI: `10.1016/j.ijhydene.2022.06.247`.

4. LEE, Howard et al. Development of flashback resistant low-emission micro-mixing fuel injector for 100% hydrogen and syngas fuels. *Proceedings of the ASME Turbo Expo*. 2009, vol. 2, pp. 411–419. ISBN 9780791848838. Available from DOI: `10.1115/GT2009-59502`.

5. SCHEFER, R. W. et al. Visible emission of hydrogen flames. *Combustion and Flame*. 2009, vol. 156, no. 6, pp. 1234–1241. ISSN 00102180. Available from DOI: `10.1016/j.combustflame.2009.01.011`.

6. WORMHOUDT, J.; YOUSEFIAN, V. Visible emission from space shuttle main engine mach disks. *Journal of Spacecraft and Rockets*. 1982, vol. 19, no. 4, pp. 382–384. ISSN 00224650. Available from DOI: `10.2514/3.62272`.

7. SCHEFER, R W et al. *Evaluation of NASA Lean Premixed Hydrogen Burner*. 2002. Tech. rep., January.

8. TINAUT, F. V. et al. Measurements of OH* and CH* chemiluminescence in premixed flames in a constant volume combustion bomb under autoignition conditions. *Energy and Fuels*. 2010, vol. 25, no. 1, pp. 119–129. ISSN 08870624. Available from DOI: `10.1021/ef1013456`.

9. TURNER, Joanna et al. A review on the ability of smartphones to detect ultraviolet (UV) radiation and their potential to be used in UV research and for public education purposes. *Science of the Total Environment*. 2020, vol. 706. ISSN 18791026. Available from DOI: `10.1016/j.scitotenv.2019.135873`.

10. ALHUYI NAZARI, Mohammad et al. Utilization of hydrogen in gas turbines: a comprehensive review. *International Journal of Low-Carbon Technologies*. 2022, vol. 17, no. March, pp. 513–519. ISSN 17481325. Available from DOI: `10.1093/ijlct/ctac025`.

11. MASLENNIKOV, V. M.; SHTERENBERG, V. Ja. Advanced gas turbine system utilizing partial oxidation technology for ecologically clean power generation. *International Journal of Low-Carbon Technologies*. 2011, vol. 6, no. 1, pp. 55–63. ISSN 17481317. Available from DOI: `10.1093/ijlct/ctq043`.

12. KANG, Hyebin; KIM, Kyu Tae. Combustion dynamics of multi-element lean-premixed hydrogen-air flame ensemble. *Combustion and Flame*. 2021, vol. 233, p. 111585. ISSN 15562921. Available from DOI: `10.1016/j.combustflame.2021.111585`.

13. CHIESA, Paolo et al. Using hydrogen as gas turbine fuel. *Journal of Engineering for Gas Turbines and Power*. 2005, vol. 127, no. 1, pp. 73–80. ISSN 07424795. Available from DOI: `10.1115/1.1787513`.

14. SHIN, Youngjun; CHO, Eun-Seong. Numerical Study on H Enriched NG Lean Premixed Combustion. *Journal of The Korean Society of Combustion*. 2021, vol. 26, no. 1, pp. 51–58. ISSN 1226-0959. Available from DOI: `10.15231/jksc.2021.26.1.051`.

15. CHO, Eun-Seong et al. A novel 100% hydrogen gas turbine combustor development for industrial use. *Turbomachinery Technical Conference and Exposition GT2022*. 2022, pp. 1–6.

16. HERNANDEZ, Steven et al. Micro-mixing fuel injection for low emission combustion of hydrogen for gas turbine applications. *25th Annual International Pittsburgh Coal Conference, PCC - Proceedings*. 2008. ISBN 189097725X.

17. WU, Y. et al. Prediction of the liftoff, blowout and blowoff stability limits of pure hydrogen and hydrogen/hydrocarbon mixture jet flames. *International Journal of Hydrogen Energy*. 2009, vol. 34, pp. 5940–5945.

18. KUO, Kenneth K. Principles of Combustion. In: *Principles of combustion*. 2nd. Wiley, 2005, pp. 484–485. ISBN 978-0-471-04689-9.

19. TENG, Fei. *The Effect of Hydrogen Concentration on the Flame Stability and Laminar Burning Velocity of Hydrogen-Hydrocarbon-Carbon Dioxide Mixtures*. 2014. PhD thesis.

20. SCHEFER, R. W. Hydrogen enrichment for improved lean flame stability. *International Journal of Hydrogen Energy*. 2003, vol. 28(10), pp. 1131–1141.

21. GRIEBEL, Peter et al. Lean blowout limits and NOx emissions of turbulent, lean premixed, hydrogen-enriched methane/air flames at high pressure. *Journal of Engineering for Gas Turbines and Power*. 2007, vol. 129, no. 2, pp. 404–410. ISSN 07424795. Available from DOI: `10.1115/1.2436568`.

22. SCHEFER, R.W. et al. Combustion of hydrogen-enriched methane in a lean premixed swirl-stabilized burner. *Proceedings of the Combustion Institute*. 2002, vol. 29, pp. 843–851.

23. WICKSALL, D.M. et al. Fuel composition effects on the velocity field in a lean premixed swirl-stabilized combustor. *ASME Turbo Expo 2003 Power for Land, Sea, and Air*. 2003.

24. WICKSALL, D.M. et al. The interaction of flame and flow field in a lean premixed swirl-stabilized combustor a¡operated on H2/CH4/air. *Proceedings of the Combustion Institute2*. 2005, vol. 30, pp. 2875–2883.

25. NGUYEN, O.; SAMUELSEN, S. The effect of discrete pilot hydrogen dopant injection on the lean blowout performance of a model gas turbine combustor. *The International Gas Turbine and Aeroengine Congress and Exhibition*. 1999.

26. JACKSON, G.S. et al. Influence of H2 on the response of lean premixed CH4 flames to high strained flows. *Combustion and Flame*. 2003, vol. 132, pp. 503–511.

27. REN, J.-Y. et al. Brief Communication: Strain-rate effects on hydrogen-enhanced lean premixed combustion. *Combustion and Flame*. 2001, vol. 124, pp. 717–720.

28. GUO, H.S. et al. The effect of hydrogen addition on flammability limit and NOx emission in ultra-lean counterflow CH4/air premixed flame. *Proceedings of the Combustion Institute2*. 2005, vol. 30, pp. 303–311.

29. VANCE, Faizan Habib et al. Flame stabilization and blow-off of ultra-lean H2-air premixed flames. *Energies*. 2021, vol. 14, no. 7. ISSN 19961073. Available from DOI: `10.3390/en14071977`.

30. SETTLES, Gary S.; HARGATHER, Michael J. A review of recent developments in schlieren and shadowgraph techniques. *Measurement Science and Technology*. 2017, vol. 28, no. 4, aa5748. ISSN 13616501. Available from DOI: `10.1088/1361-6501/aa5748`.

31. KAISER, Sebastian Arnold et al. Schlieren measurements in the round cylinder of an optically accessible internal combustion engine. *Applied Optics*. 2013, vol. 52, no. 14, pp. 3433–3443. ISSN 15394522. Available from DOI: `10.1364/AO.52.003433`.

32. JI, Longjuan et al. Effect of confinement ratio on flame structure and blow-off characteristics of swirl flames. *Experimental Thermal and Fluid Science*. 2022, vol. 135, no. July 2021, p. 110630. ISSN 08941777. Available from DOI: `10.1016/j.expthermflusci.2022.110630`.

33. YANG, Jiabao et al. Experimental studies of the effects of global equivalence ratio and CO2 dilution level on the OH* and CH* chemiluminescence in CH4/O2 diffusion flames. *Fuel*. 2020, vol. 278, no. May. ISSN 00162361. Available from DOI: `10.1016/j.fuel.2020.118307`.

34. GAYDON, A.G. The spectroscopy of flames. *Springer: New York*. 1974.

35. GILBLOM, David L.; YOO, Sang Kuen. Infrared and ultraviolet imaging with a CMOS sensor having layered photodiodes. *Sensors and Camera Systems for Scientific, Industrial, and Digital Photography Applications V*. 2004, vol. 5301, no. Figure 1, p. 186. ISSN 0277786X. Available from DOI: `10.1117/12.528427`.

36. WILKES, Thomas C. et al. Ultraviolet imaging with low cost smartphone sensors: Development and application of a raspberry pi-based UV camera. *Sensors (Switzerland)*. 2016, vol. 16, no. 10. ISSN 14248220. Available from DOI: `10.3390/s16101649`.

37. TELEDYNE PRINCETON INSTRUMENTS. *Sensor Improvements to Enhance UV Sensitivity from 10 - 400 nm*. 2022. Available also from: `https://www.princetoninstruments.com/learn/camera-fundamentals/sensor-improvements-to-enhance-uv-sensitivity-from-10-400-nm`.

38. PHOTONICS. *Ultraviolet Reflectance Imaging: Applications*. 2022. Available also from: `https://www.photonics.com/Articles/Ultraviolet_Reflectance_Imaging_Applications/a32169`.

39. SONY SEMICONDUCTOR SOLUTIONS CORPORATION. *IMX487-AAMJ*. 2021.

40. DYNACOLOR. *USB3 Vision camera series FB-N9-U*. [N.d.]. No. 15.

41. ANDOR TECHNOLOGY. *andor*. Hardware Guide for the iStar Intensified sCMOS camera. 2017.

42. LIU, Yize et al. Review of modern low emissions combustion technologies for aero gas turbine engines. *Progress in Aerospace Sciences*. 2017, vol. 94, no. September, pp. 12–45. ISSN 03760421. Available from DOI: `10.1016/j.paerosci.2017.08.001`.

43. LIU, Yao et al. Experimental investigation of chemiluminescence and NOx emission characteristics in a lean premixed dual-swirl flame. *Case Studies in Thermal Engineering*. 2021, vol. 28, no. October, pp. 4–12. ISSN 2214157X. Available from DOI: `10.1016/j.csite.2021.101653`.

44. ZHANG, Meng et al. The regulation effect of methane and hydrogen on the emission characteristics of ammonia/air combustion in a model combustor. *International Journal of Hydrogen Energy*. 2021, vol. 46, no. 40, pp. 21013–21025. ISSN 03603199. Available from DOI: `10.1016/j.ijhydene.2021.03.210`.

45. WANG, Zhichao et al. Experimental study on NOx emission correlation of fuel staged combustion in a LPP combustor at high pressure based on NO-chemiluminescence. *Chinese Journal of Aeronautics*. 2020, vol. 33, no. 2, pp. 550–560. ISSN 10009361. Available from DOI: `10.1016/j.cja.2019.09.004`.

46. MAHMUD, R. et al. Characteristics of Flat-Wall Impinging Spray Flame and Its Heat Transfer under Small Diesel Engine-Like Condition. 3th Report: Effect of Oxygen Concentration. *IOP Conference Series: Materials Science and Engineering*. 2019, vol. 462, no. 1. ISSN 1757899X. Available from DOI: `10.1088/1757-899X/462/1/012046`.

47. SICK, Volker. High speed imaging in fundamental and applied combustion research. *Proceedings of the Combustion Institute*. 2012, vol. 34, no. 2, pp. 3509–3530. ISSN 15407489. Available from DOI: `10.1016/j.proci.2012.08.012`.

48. SUN, Duo et al. Flame stability monitoring and characterization through digital imaging and spectral analysis. *Measurement Science and Technology*. 2011, vol. 22, no. 11. ISSN 13616501. Available from DOI: `10.1088/0957-0233/22/11/114007`.

49. LU, Gang et al. A digital imaging based multifunctional flame monitoring system. *IEEE Transactions on Instrumentation and Measurement*. 2004, vol. 53, no. 4, pp. 1152–1158.

50. YAN, Y. et al. Monitoring and characterisation of pulverised coal flames using digital imaging techniques. *Fuel*. 2002, vol. 81, no. 5, pp. 647–655. ISSN 00162361. Available from DOI: `10.1016/S0016-2361(01)00161-2`.

51. LU, Gang et al. Concurrent measurement of temperature and soot concentration of pulverized coal flames. *IEEE Transactions on Instrumentation and Measurement*. 2002, vol. 51, no. 5, pp. 990–995. ISSN 00189456. Available from DOI: `10.1109/TIM.2002.807804`.

52. EL-GHAFOUR, S. A.A. et al. Combustion characteristics of natural gas-hydrogen hybrid fuel turbulent diffusion flame. *International Journal of Hydrogen Energy*. 2010, vol. 35, no. 6, pp. 2556–2565. ISSN 03603199. Available from DOI: `10.1016/j.ijhydene.2009.12.049`.

53. MATHWORKS. *What Is Image Recognition?* 2023. Available also from: `https://www.mathworks.com/discovery/image-recognition-matlab.html`.

54. MATHWORKS. *Image Labeler - Label images for computer vision applications*. 2023. Available also from: `https://www.mathworks.com/help/vision/ref/imagelabeler-app.html`.

55. KROGH, Anders. What are artificial neural networks? *Nature Biotechnology*. 2008, vol. 26, no. 2, pp. 195–197. ISSN 10870156. Available from DOI: `10.1038/nbt1386`.

56. ZHANG, Zhihua. *Multivariate Time Series Analysis in Climate and Environmental Research*. Multivariate Time Series Analysis in Climate and Environmental Research. Springer, 2017. ISBN 9783319673400. Available from DOI: `10.1007/978-3-319-67340-0`.

57. ZHANG, Cha; MA, Yunqian. *Ensemble Machine Learning*. Ensemble Machine Learning. 2012. ISBN 9781441993250. Available from DOI: `10.1007/978-1-4419-9326-7`.

58. BREIMAN, L. Random Forests. *2021 IEEE International Conference on Consumer Electronics and Computer Engineering, ICCECE 2021*. 2001, pp. 542–545. ISBN 9781728183190. Available from DOI: `10.1109/ICCECE51280.2021.9342376`.

59. PISNER, Derek A.; SCHNYER, David M. *Machine Learning: Methods and Applications to Brain Disorders*. Support vector machine. Elsevier Inc., 2019. ISBN 9780128157398. Available from DOI: `10.1016/B978-0-12-815739-8.00006-7`.

60. O'KEEFE CONTROLS CO. Choked Flow of Gases. 2000, vol. 1, no. 203, pp. 16, 38.

61. BROOKS INSTRUMENT. Model 5851i. Installation and Operation Manual. 2009.

62. BROOKS INSTRUMENT. Operating Manual Brooks Microprocessor Control & Read Out Unit. 2002, no. January, pp. 1–40.

63. RICHARDS, Austin. Near-UV Reflectance Imaging : Applications. *The 2008 photonics handbook*. 2008, pp. 89–92.

64. KLINE, S.; MCCLINTOCK, F. Describing unvertaities in single-sample experiments. *Mechanical engineering*. 1953, vol. 75, pp. 3–8.

65. TURNS, S. R. *An introduction to combustion: Concepts and applications*. Boston: McGraw Hill, 2000.

66. ANDERSON, David N. *Emissions of oxides of nitrogen from an experimental premixed-hydrogen burner*. Cleveland, Ohio, 1976. Tech. rep.

67. TRAN, Britney et al. Emissions and flame structure assessment of aeroengine micromixing injectors for lean direct injection of hydrogen and hydrogen/natural gas blends. *ASME Turbo Expo 2023*. 2023.